DECAY DETECTOR FOR THE STUDY OF GIANT MONOPOLE RESONANCE IN UNSTABLE NUCLEI

A Thesis

by

JONATHAN THOMAS BUTTON

Submitted to the Office of Graduate Studies of
Texas A&M University
in partial fulfillment of the requirements for the degree of

MASTER OF SCIENCE

Approved by:

Chair of Committee,	Dave H. Youngblood
Committee Members,	Sherry J. Yennello
	Che-Ming Ko
	Joseph H. Ross, Jr.
Head of Department,	George R. Welch

May 2013

Major Subject: Physics

ABSTRACT

Giant Resonances (GR) are the broad resonances that occur at excitation energies between 10 and 30 MeV. They correspond to the collective motion of nucleons within the nucleus. The GR modes can be classified according to their multipolarity L, spin S and isospin T quantum numbers. In the microscopic description, the GR modes can be understood as the collective particle-hole excitations characterized by certain values of the angular momentum and parity (J^{π}), orbital momentum, spin, and isospin.

The Giant Monopole Resonance (GMR) is interesting because its excitation energy is directly related to the incompressibility of the nucleus K_A. K_A can be used to derive the incompressibility of nuclear matter K_{NM}, but this extrapolation from the data for real nuclei is not straightforward due to contributions from surface, Coulomb and asymmetry effects. Thus, improvements to the extrapolated K_{NM} can be made by measuring the GMR for increasing (N-Z)/A. The incompressibility of nuclear matter is of importance in the nuclear equation of state (EOS) which describes a number of phenomena: collective excitations of nuclei, supernova explosions and radii of neutron stars.

In order to study the Isoscalar Giant Monopole Resonance in unstable nuclei, a ΔE-ΔE-E decay detector composed of plastic scintillator arrays has been built and tested. The measurement of the ISGMR in unstable nuclei will be done using inverse kinematics, with a 40 MeV per nucleon beam of the unstable nucleus incident on a ^{6}Li target. Xinfeng Chen studied the viability of this approach, taking data for elastic

scattering and inelastic scattering to low-lying states and giant resonances of 240 MeV ^{6}Li ions on ^{24}Mg, ^{28}Si, and ^{116}Sn.

Nuclei excited to the GMR region are particle unstable, and will decay by p, α or n decay shortly after excitation. To reconstruct the event it is necessary to measure the energy and angle of the decay particle and of the residual heavy ion. In many lighter nuclei a few nucleons off stability, and in light proton rich nuclei, the neutron threshold is above the region of interest.

DEDICATION

This Thesis is dedicated to my wife Elisabeth, son Luke, and parents Marc and Lita.

ACKNOWLEDGEMENTS

I would like to thank my committee chair, Dr. Youngblood, and my committee members, Dr. Ko, Dr. Ross, and Dr. Yennello.

Special thanks to Robert Polis, Dr. Krishichayan, and Dr. Lui for their assistance in the design, construction, and operation of our Decay Detector.

TABLE OF CONTENTS

LIST OF FIGURES

LIST OF TABLES

1. ISGMR DECAY PRODUCTS AND 3-BODY KINEMATICS

1.1 Introduction

In order to demonstrate the utility of the decay detector for measuring the giant monopole resonance (GMR) in unstable nuclei using reverse kinematics, a measurement of the GMR in ^{28}Si will be done using a 40 MeV/u beam of ^{28}Si incident upon a ^{6}Li target.

The GMR in ^{28}Si has a centroid energy of 21.5±0.3 MeV and a root mean square width of 5.9±0.2MeV. [1] In this range of excitation energy, the GMR is particle unstable and may decay by any of a number of modes (TABLE I). In sd-shell nuclei, direct decay by proton and α particles accounts for 40-80% of the total strength because for such nuclei, the Coulomb barrier is small. [2]

TABLE I: Allowed decay modes for ^{28}Si excited to GMR.

Decay Particle	Q-Value (MeV)
n	-17.1798
p	-11.5851
d	-22.4182
^{3}He	-23.2312
α	-9.98415
^{5}Li	-23.6418

There are 3 bodies in the final state (recoiling ^{6}Li, decay particle, and residual heavy ion). The recoiling ^{6}Li have low energy and for the most part will not get out of the target. Thus in order to experimentally determine the kinematics, we must measure at least three of the four quantities [3]: decay particle energy and angle, and residual nucleus energy and angle. A hole in the decay detector with a horizontal and vertical angular acceptance of 4° allows the residual heavy-ion to enter the MDM spectrometer, which has a horizontal and vertical angular acceptance of $\pm 2^{o}$. The heavy-ions energy and angle will be determined with the focal plane detector. The layout of the decay detector, MDM spectrometer, and focal plane detector is shown in FIG. 1. The decay detector can measure decay particles within an angular range of 4° to 45° with respect to the beam direction. The upper limit of 45° is more than sufficient because the maximum angle of the decay particle at relevant excitation energies is less than 40°. In the following sections, the 3-body kinematics for excitation of the GMR in ^{28}Si with subsequent decay into ^{27}Al +p and ^{24}Mg + α channels are presented.

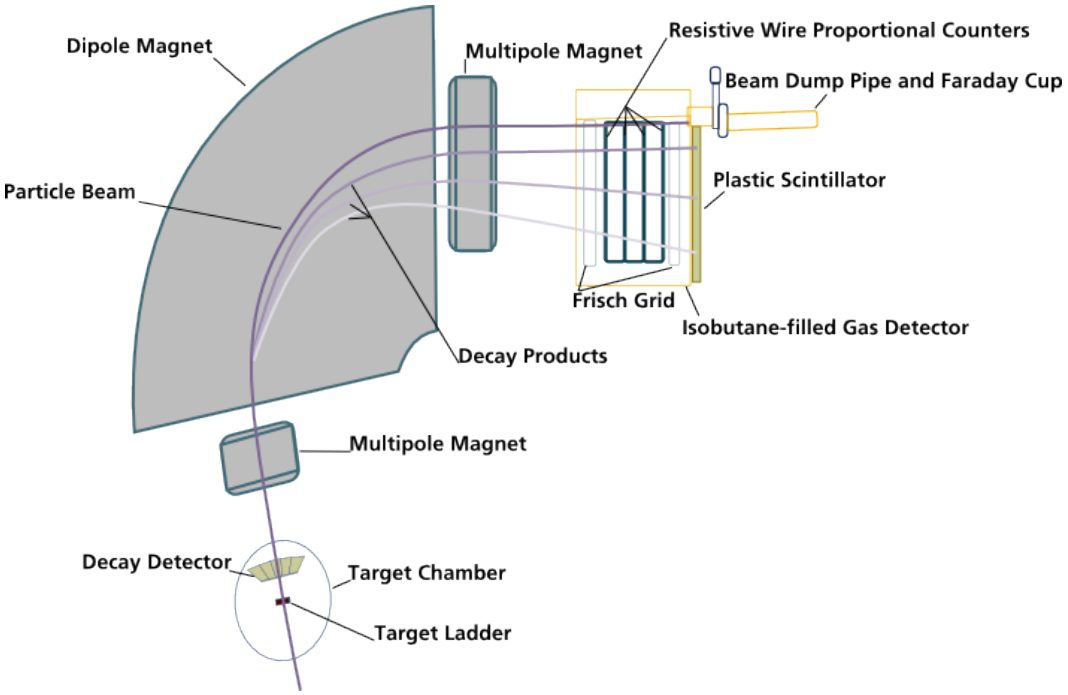

FIG. 1. Diagram of the experiment layout.

.

1.2 Calculation Method

The reaction is a sequential process (FIG. 2): first inelastic scattering occurs with 2 bodies in the final state (^{28}Si* and ^{6}Li), and then ^{28}Si* decays into ^{27}Al +p. For the inelastic scattering, the five unknown physical observables resulting from the collision of the 40 MeV/u ^{28}Si beam with the ^{6}Li target are the angles for both nuclei (θ_{6Li}, θ_{28Si*}), the final kinetic energies of both nuclei (T_{6Li}, T_{28Si*}), and the excitation energy, E_x, of the ^{28}Si*. Three equations are obtained from the relation for the relativistic momentum with

respect to T (EQ. (1)), the total relativistic energy (EQ. (2)), and the conservation of both the momentum and the energy (EQ'S. (3) and (4)). Applying a similar procedure with EQ'S. (5) and (6) to the decay of the recoil nucleus yields three additional equations and four additional unknown quantities (θ_H, θ_L, T_H, T_L). The rest mass is m_0, and c is the speed of light.

$$(pc)^2 = T^2 + 2Tm_0c^2 \tag{1}$$

$$E = T + m_0c^2 \tag{2}$$

$$\vec{p}_{28Si} = \vec{p}_{28Si^*} + \vec{p}_{6Li} \tag{3}$$

$$T_{28Si} = T_{28Si^*} + E_x + T_{6Li} \tag{4}$$

$$\vec{p}_{28Si^*} = \vec{p}_1 + \vec{p}_2 \tag{5}$$

$$T_{28Si^*} + T_x = T_H + T_L \tag{6}$$

The kinematically allowed combinations of energy and angle for the target nucleus and two decay nuclei at varying values of E_x were found by sampling random combinations of θ_{28Si*} and θ_H (where θ_H is the angle of the heavy decay nucleus) then numerically solving (by Newton's method for a system of nonlinear equations, adapted from published code [4]) for the remaining unknown quantities from the collision and resonance excitation (θ_{6Li}, T_{28Si*}, and T_{6Li}) and the decay (θ_L, T_H, T_L). All angles θ are in the lab-frame, with respect to the incident beam direction.

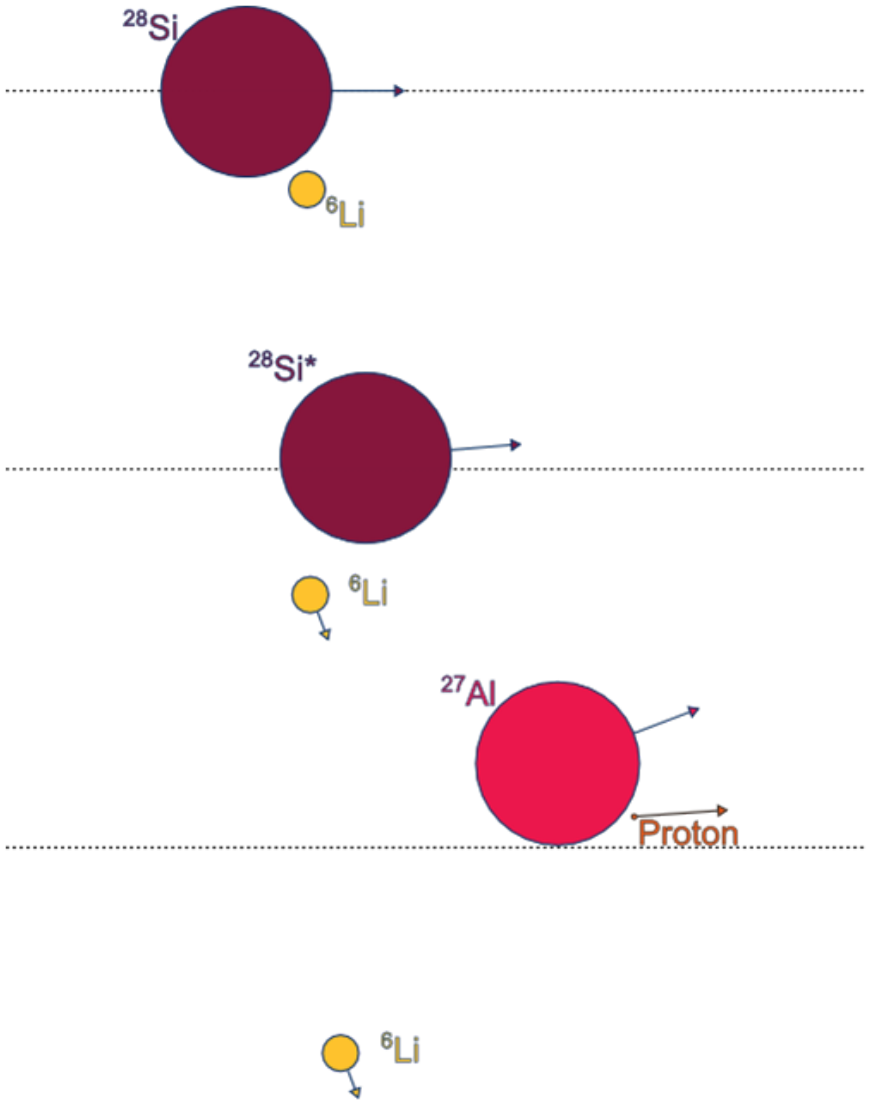

FIG. 2. A Representation of the decay kinematics as seen in the lab-frame: 1120 MeV ^{28}Si collides with the ^{6}Li target. In this example, the excited ^{28}Si* then decays to p+^{27}Al.

The maximum values for θ_{28Si*} and θ_H can be found by considering the collision and decay in the center-of-mass frame.[5] In the case of the two-particle system described above, in the lab frame, the invariant magnitude of the momentum 4-vector (s) is written as

$$s = \left(\sum_i E_i\right)^2 - \left(\sum_i \vec{p}_i\right)^2 = (m_{6Li} + m_{28Si})^2 + 2m_{6Li}T_{28Si}. \quad (7)$$

Writing EQ. (7) in terms of the center-of-mass momentum gives

$$s = \left(\sqrt{m_{6Li}^2 + p_{cm}^2} + \sqrt{m_{28Si}^2 + p_{cm}^2}\right)^2. \quad (8)$$

Then solving for the center-of-mass momentum gives

$$p_{cm}^2 = \frac{\left(s - m_{6Li}^2 - m_{28Si}^2\right)^2 - 4m_{6Li}^2 m_{28Si}^2}{4s}. \quad (9)$$

The rapidity, φ, is the hyperbolic angle between two reference frames in relative motion. The Lorentz transformation can be written in terms of φ,

$$\begin{pmatrix} E_{lab} \\ p_{lab} \end{pmatrix} = \begin{pmatrix} \cosh\varphi & -\sinh\varphi \\ -\sinh\varphi & \cosh\varphi \end{pmatrix} \begin{pmatrix} E_{cm} \\ p_{cm} \end{pmatrix}. \quad (10)$$

From this equation, the center-of-mass rapidity can be calculated by considering the transformation of the ^{6}Li target prior to the collision from the lab frame into the center-of-mass frame,

$$\boldsymbol{\varphi = \ln\left(\frac{p_{cm} + \sqrt{m_{6Li}^2 + p_{cm}^2}}{m_{6Li}}\right)}. \quad (11)$$

Following the collision, in the center of mass frame, the momenta of the ^{28}Si and the ^{6}Li are equal and opposite ($p_{\mathrm{f,cm}}$). EQ. (10) is then used again to find the energy and momentum for both particles EQS.(12) - (14), where ∥ refers to the direction of the relative velocity of the reference frame and ⊥ refers to the direction perpendicular to the relative velocity of the reference frame.

$$E_{lab} = \sqrt{p_{f,cm}^2 + m^2}\cosh\varphi - p_{f,cm}\cos\theta_{f,cm}\sinh\varphi \tag{12}$$

$$\boldsymbol{p_{\parallel} = p_{lab}\cos\theta_{lab} = \pm p_{f,cm}\cos\theta_{f,cm}\cosh\varphi + \sqrt{p_{f,cm}^2 + m^2}\sinh\varphi} \tag{13}$$

$$\boldsymbol{p_{\perp} = p_{lab}\sin\theta_{lab} = p_{f,cm}\sin\theta_{f,cm}} \tag{14}$$

Combining EQ'S. (13) - (14) in order to solve for p_{lab} in terms of θ_{lab} yields the following condition on the lab angle:

$$p_{f,cm} < m\sinh\varphi\sin\theta_{lab}.$$

For mass *m* that is sufficiently large, there is a maximum allowed scattering angle. In the case of the 1120 MeV ^{28}Si bombarding a ^{6}Li target, the maximum allowed scattering angle in the lab frame for the ^{28}Si is approximately 12.4°. Applying these steps to the case where the ^{28}Si is excited into the GMR and then decays by p+^{27}Al or α+^{24}Mg, the maximum scattering angle for the heavy decay nucleus can also be calculated (FIG. 3).

Calculation of the angular distributions of the cross section for ^{6}Li inelastic scattering on ^{28}Si target shows that the monopole resonance can be distinguished from

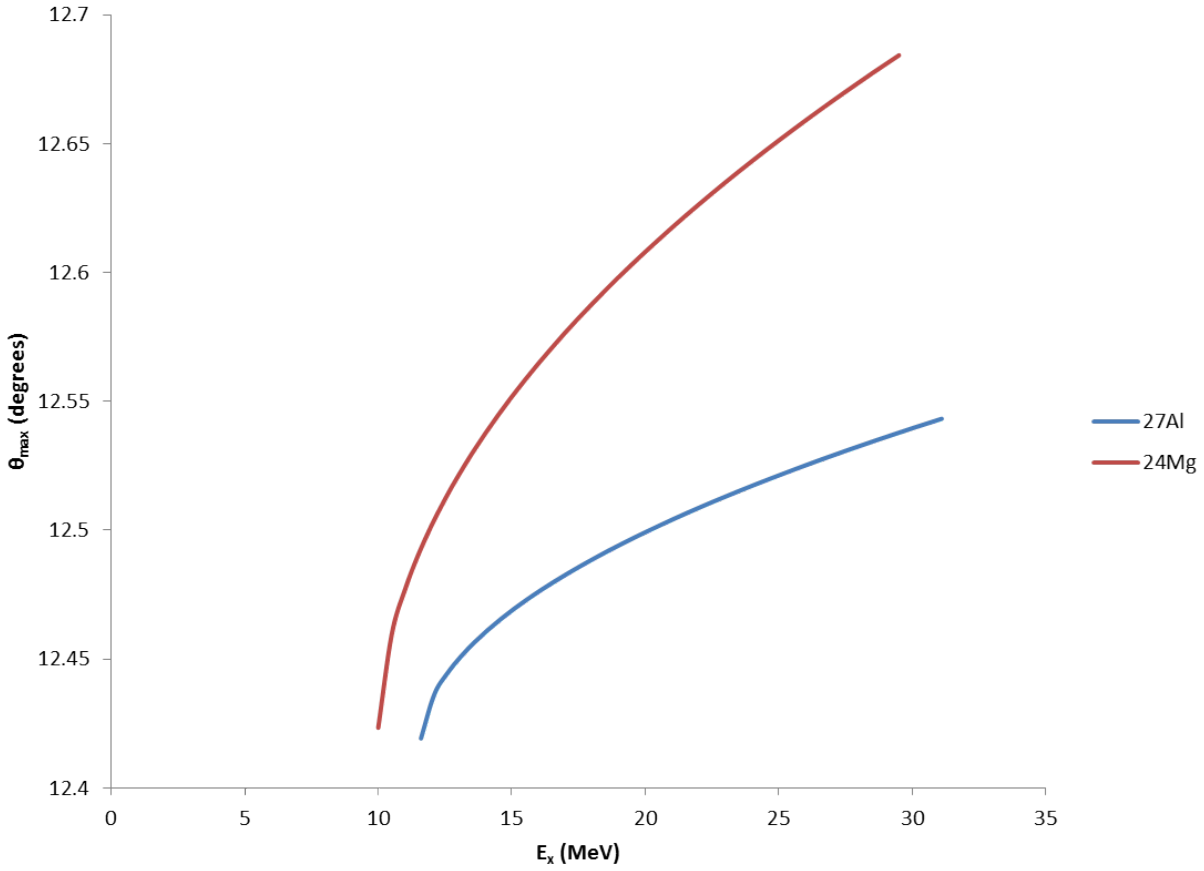

FIG. 3. Plot of the maximum scattering angle in the lab frame as a function of excitation energy of ^{28}Si.

the quadrupole using, at a minimum, data taken over an angular range in the center of mass frame of 0° to 4° [6]. In the 40 MeV/u reverse kinematics, this corresponds to a

range of the ^{28}Si lab angle, θ_{lab}:0° to 1.1°. The angular range of the spectrometer is 0° to 2°.

.

1.3 Phase Space for Energy and Angle of the GMR Decay Products

Using the method described in the last section, plots of the energy and angle phase space of the GMR decay particles were produced for different combinations of excitation energy and decay channel. The calculation was restricted to the angular range of interest, 0° to 2°, for the heavy decay nucleus (either ^{27}Al or ^{24}Mg). The kinematic range of the decay particles is listed in TABLE II. The angular range of the light decay particles fall within the limits of the decay detector. Protons having energies less than 9.2 MeV or greater than 73.6 MeV will be outside the detection limit. The decay detector covers the entire energy range of the α particles.

TABLE II: The kinematic range for the decay particles at different excitation energies.

Decay Channel	Excitation Energy (MeV)	Θ_L Range	T_H Range (MeV)	T_L Range (MeV)
$\alpha+^{24}$Mg;	19	0° - 28°.	436 - 1032	69 - 263
$\alpha+^{24}$Mg,	24	0° - 18°.	861 - 1020	90 - 243
$p+^{27}$Al	19	0° - 29°.	1017 - 1096	11 - 84
$p+^{27}$Al	24	0° - 38°.	1001 - 1100	7 - 99

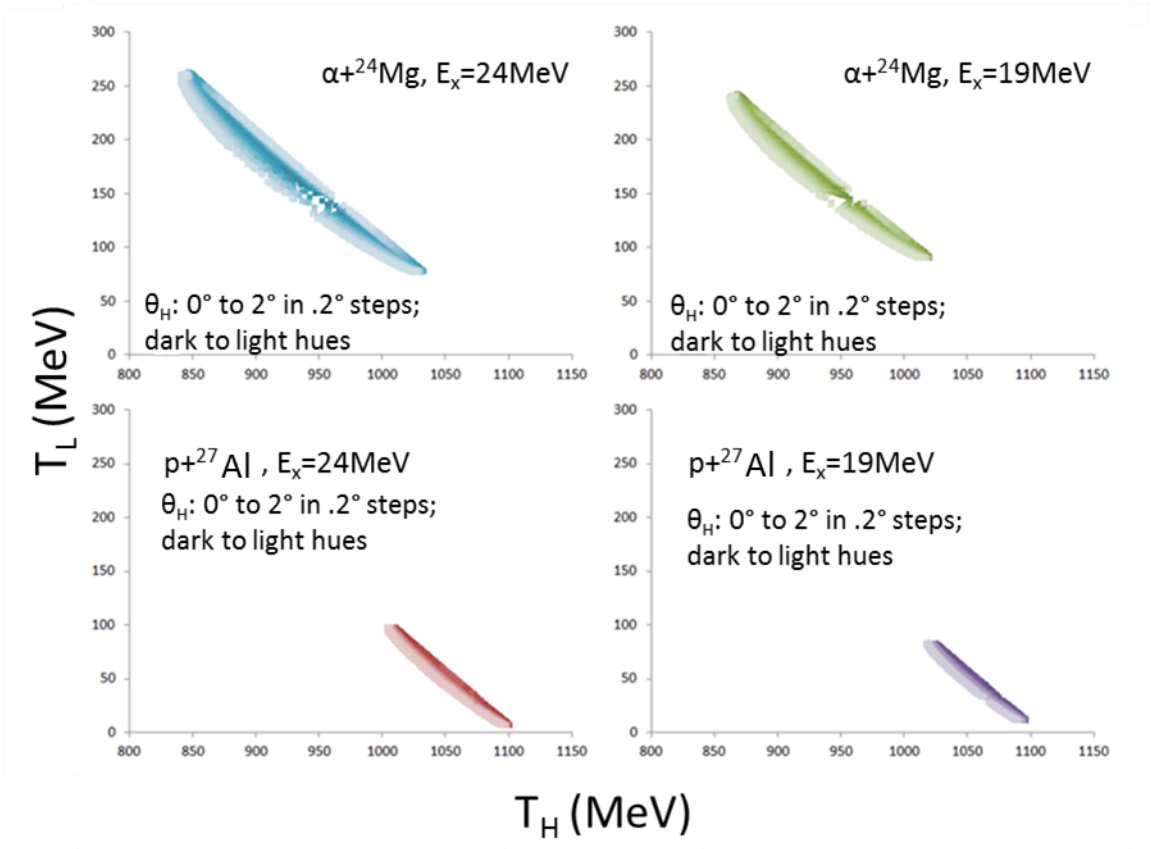

FIG. 4: Plot of the kinetic energy of the light particle (T_L) vs that of the heavy particle (T_H) for a continuous range of values for the lab scattering angle of the heavy particle (θ_H). The values for θ_H are related to the hues of the plotted points. The decay channel and excitation energy are displayed on each plot.

The relationship between T_H and T_L for varying values of excitation energy and θ_L are shown in FIG. 4. As seen in FIG. 5, the phase space for T_H and T_L gets larger with increasing angle. FIG. 6 shows the relationship between θ_L and T_L with varying excitation energy and T_H; it is a rotation of the plots in FIG. 4.

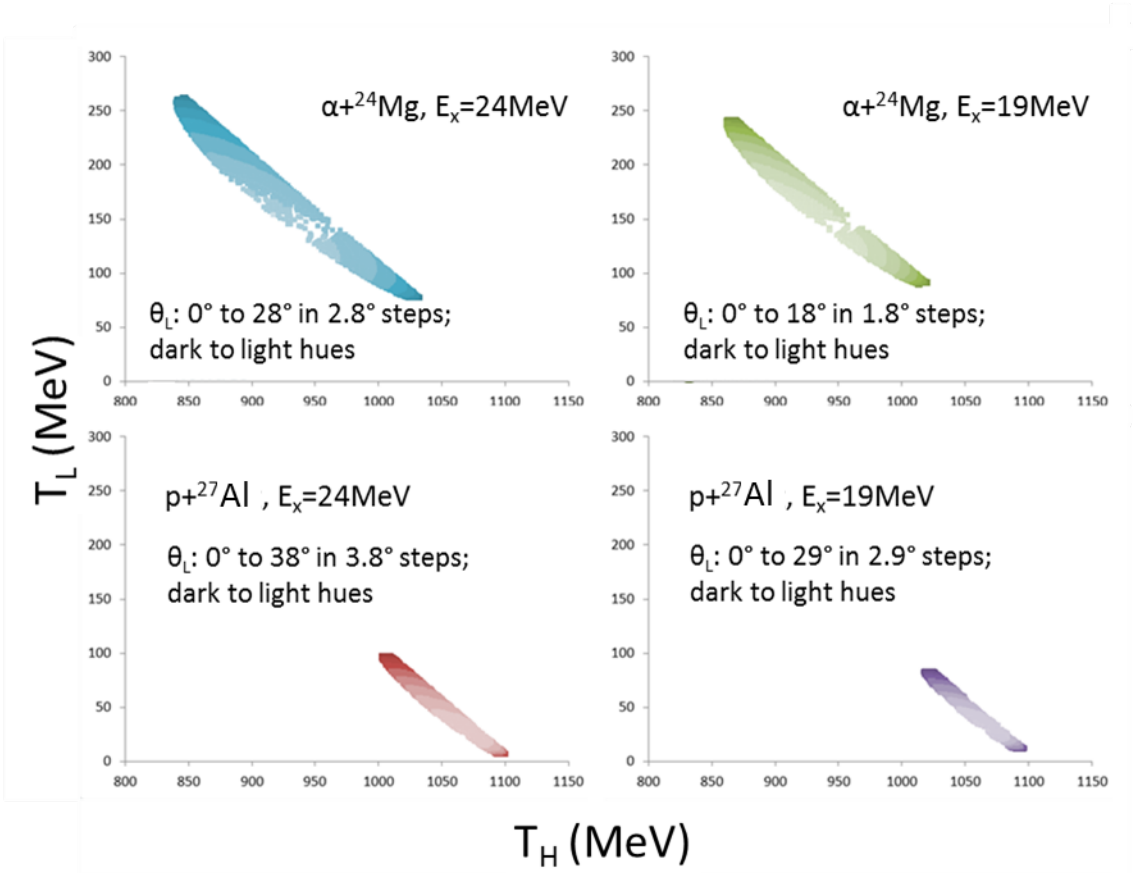

FIG. 5: Plot of T_L vs T_H for a continuous range of values for θ_L. The values for θ_L are related to the hues of the plotted points. The decay channel and excitation energy are displayed on each plot.

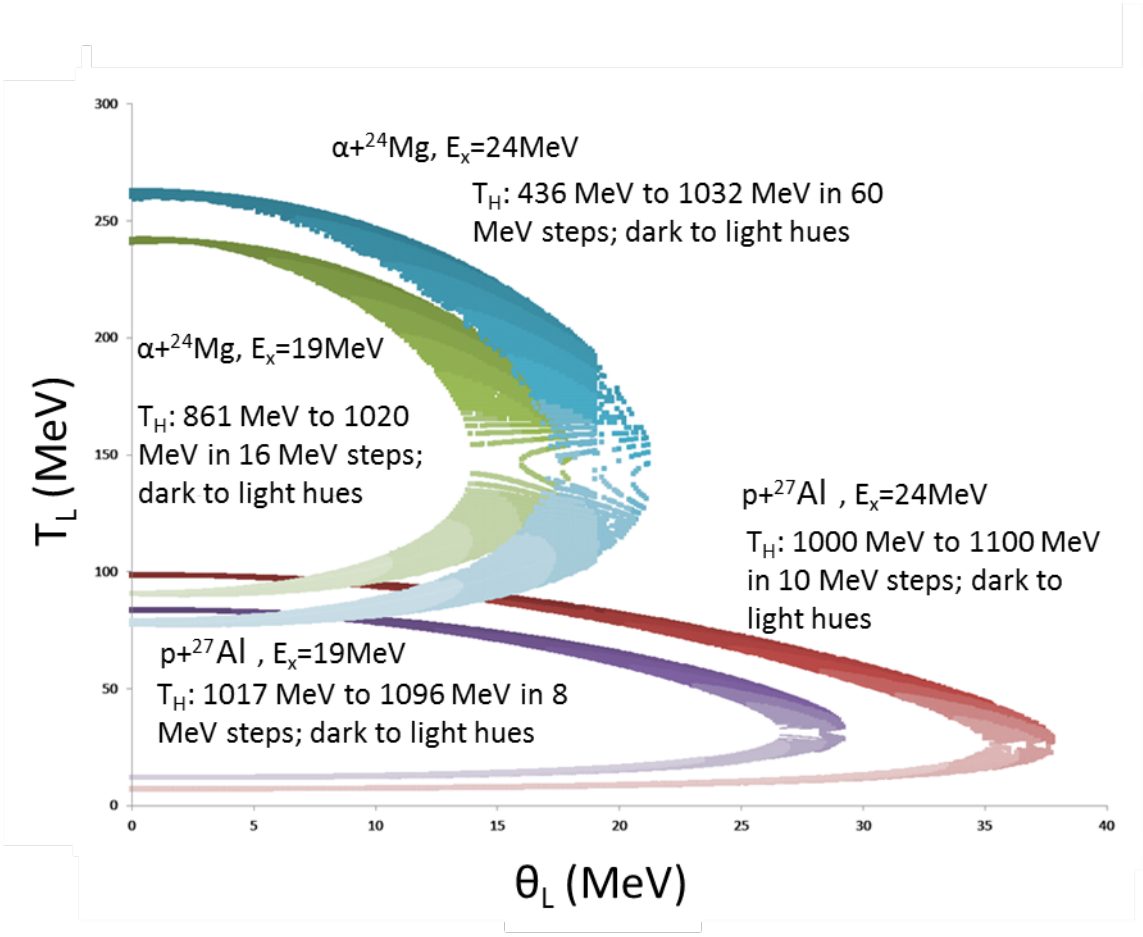

FIG. 6: Plot of T_L vs θ_L for a continuous range of values for T_H. The values for T_H are related to the hues of the plotted points. The decay channel and excitation energy are displayed on the plot.

2. ΔE-ΔE-E DECAY DETECTOR

2.1 Introduction

Nuclei excited to the ISGMR region are particle unstable, and will decay by p, α or n decay shortly after excitation. To reconstruct the event it is necessary to measure the energy and angle of the decay particle and of the residual heavy ion. In many lighter nuclei a few nucleons off stability, and in light proton rich nuclei, the neutron threshold is above the region of interest, so an array consisting of a combination of thin plastic strip scintillators and large block scintillators has been designed and constructed (FIG. 7) to measure the light charged particles from the decay of the GMR. The thin strips are in two layers, one oriented horizontally and the other oriented vertically. Coincidences between the two layers will provide the angle of the decay particle. Block scintillators are placed behind the thin strips to stop decay particles which pass through the thin strips. By summing the signals from the scintillators, the total energy of the decay particles can be determined, and by comparing this to the energy loss in the thin scintillators, different particle types can be distinguished. The scintillators are coupled to photomultiplier tubes (PMT), where the light response of the scintillators is converted into a voltage output which for a given type particle should be roughly proportional to the energy deposited by the incident particle.

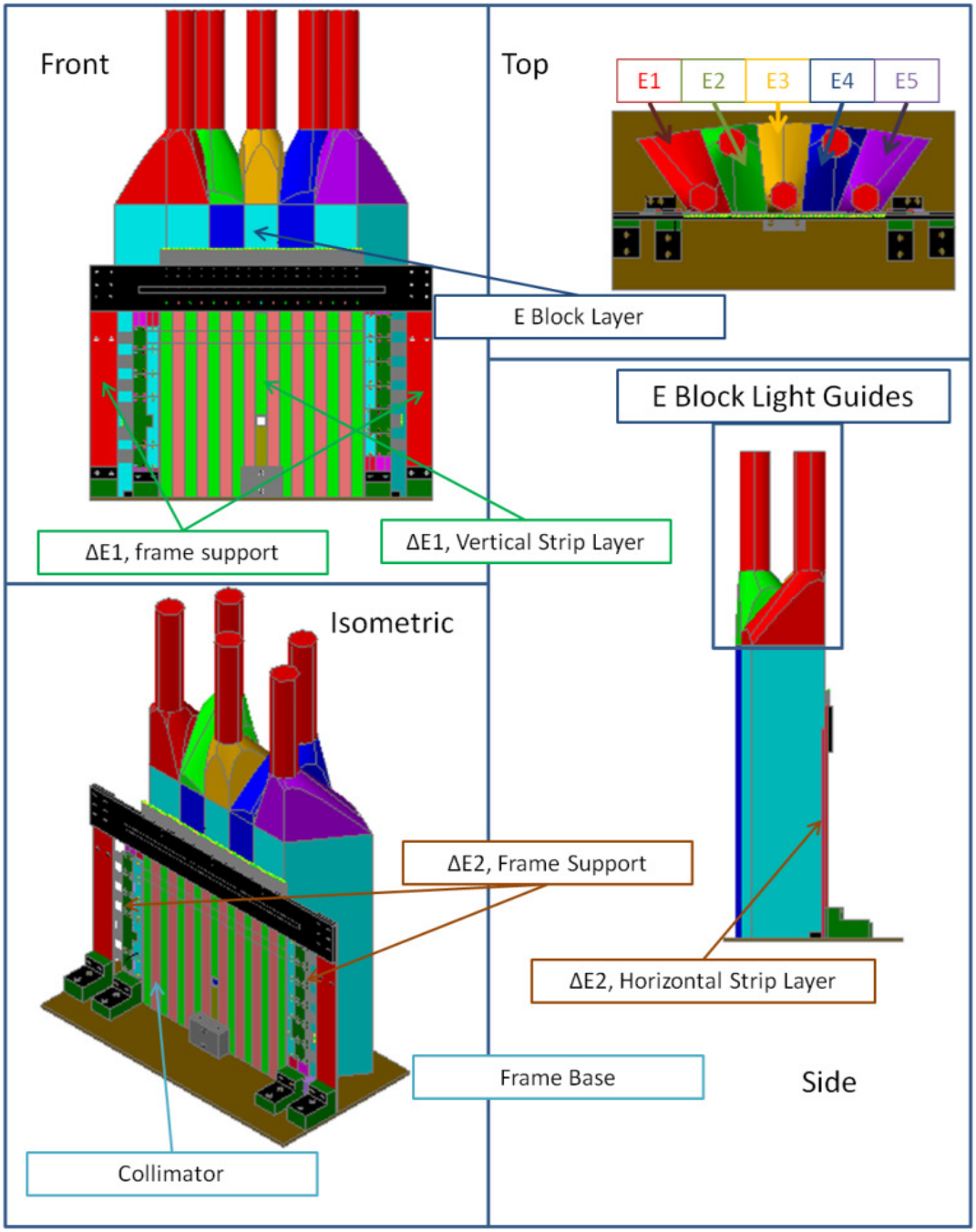

FIG. 7: Schematic of the decay detector. The front of the block scintillator array is flat and lies parallel to the scintillator strips. Each block covers ~14° relative to the beam direction. The position of each block scintillator light guide can be seen in the Top view. A brass collimator is fixed at the center-bottom position of the frame base and has a ±2°x±2° square hole through which the beam passes. One vertical (V7) and two horizontal (H9L and H9R) strips are half-length in order to accommodate the collimator. Block E3 extends from the top of the array down to the collimator and has a ±2.5° horizontal and ±1.25° vertical notch through which the beam passes.

2.2 Decay Detector Description

The decay detector is composed of 26 thin strip plastic scintillators[1] (1 mm x 1 cm x 20 cm) arranged in 2 back-to-back arrays. The ideal strip scintillator alignment is illustrated in detail in FIG. 8. In the array closest to the target, designated ΔE1, 13 scintillator strips are oriented vertically and are labeled V1 through V13, where V1 is the furthest left relative to the beam direction. V7 is centered above the beam path and is not of full-length. In the array ΔE2, 13 scintillator strips fill 12 horizontal rows labeled H1 through H12, where H1 is positioned at the top of the array. The H9 row is composed of 2 shorter length strips (H9L and H9R) located on the left and right of the beam path. Each scintillator strip is joined by optical cement[2] to a bundle of 19 optical fibers[3]. The opposite end of each fiber bundle is mated to a PMT[4].

The third layer of the decay detector, E, is composed of 5 large blocks of plastic scintillator[5] of various dimensions (the footprint of which can be seen in the Top view in FIG. 7). Four blocks (E1, E2, E4, and E5) have a height of 25 cm. The middle block, E3, has a height of 18.7 cm and extends over the beam path. It has a rectangular notch (FIG. 9) cut into its bottom in order to allow beam particles with angle less than ±2.5° to pass into the MDM spectrometer. The light guide for each block extends through the lid of the target chamber and is mated to a PMT[6].

---

[1] Saint Gobain, BC-408
[2] Saint Gobain, BC-600
[3] Saint-Gobain, BCF-91A
[4] Hamamatsu, R1635
[5] Saint Gobain, BC-408
[6] Hamamatsu, R1759

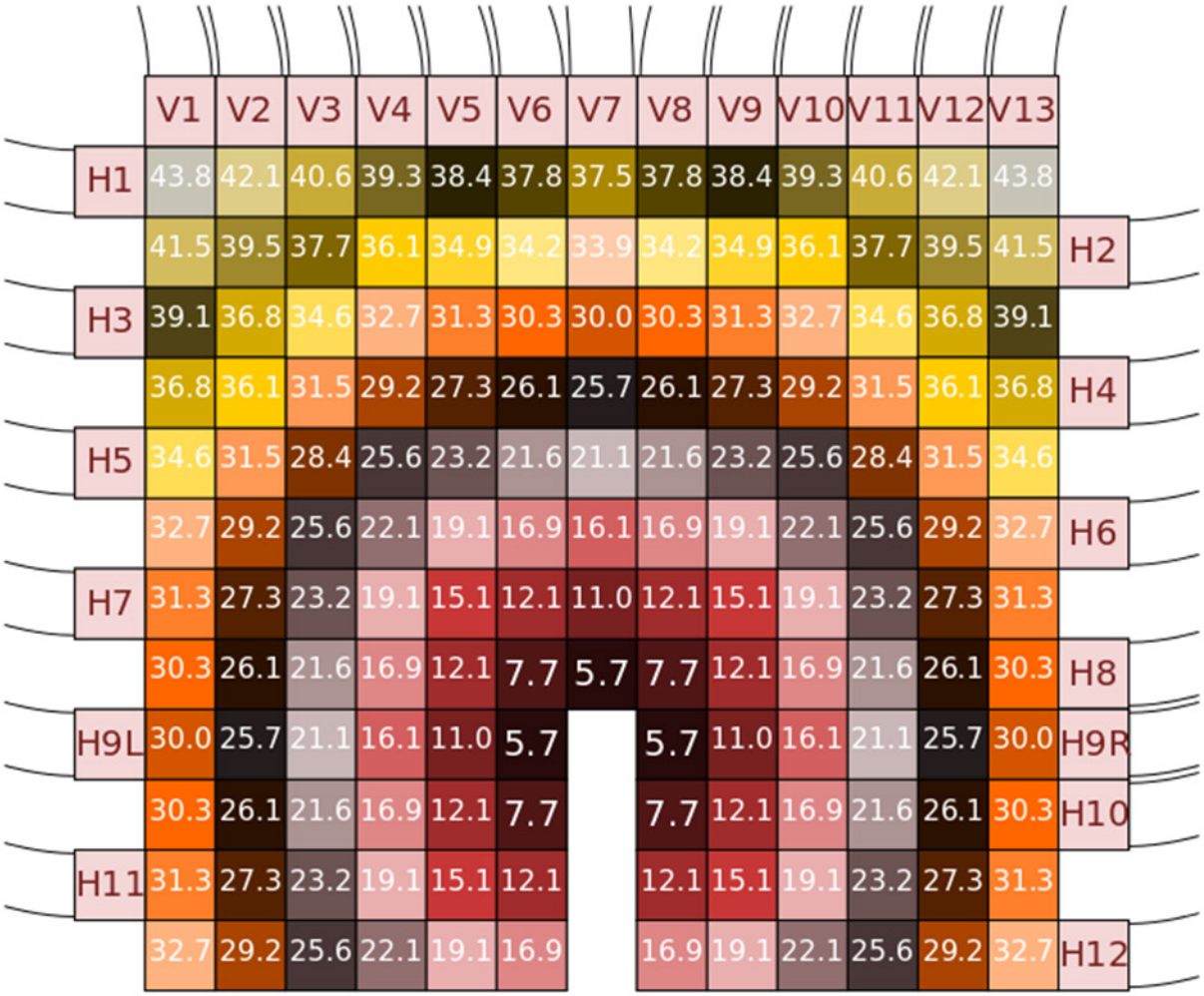

FIG. 8: A map of the ideal ΔE1-ΔE2 pixel geometry. The median accepted azimuthal angle in degrees (with respect to beam direction) is overlaid on each pixel color-coded by angle. The label location (e.g. H1 on the left of the array) for each vertical and horizontal strip indicates the location of the optical connection of the scintillator with its fiber bundle. H10,11, and 12 are full length strips; the break in the figure indicates the location of the brass collimator which extends down to the frame base.

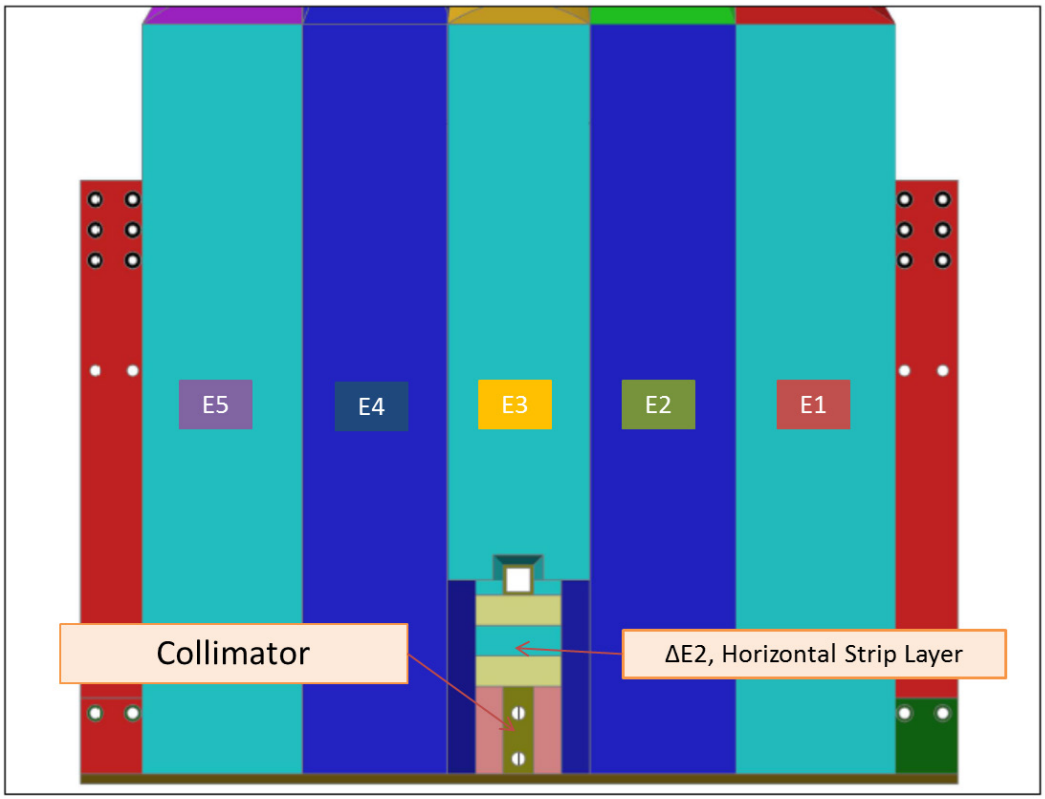

FIG. 9: Schematic of the back view of the decay detector. The channel cut into the bottom of block E3 and several elements of the ΔE2 layer are visible.

2.3 Energy and Angle Acceptance

Ions lose energy in materials in a characteristic way dependent on charge and nucleon number. Plotting curves of energy loss (ΔE) in the thin scintillators versus total energy (E) allows for particle identification for a range of energies of ions incident upon the decay detector where either the ion is stopped in the ΔE2 layer or in the E layer.

TABLE III: Maximum energy incident on the decay detector such that the ion is stopped in one of the layers of scintillator (ΔE1, ΔE2, or E-block) [7].

Layer	p (MeV)	d (MeV)	t (MeV)	^{3}He (MeV)	α (MeV)	^{6}Li (MeV)
ΔE1	9.2	12.4	14.8	32.3	36.7	69.2
ΔE2	13.5	18.3	21.9	47.5	54.0	101.7
E-block	73.6	100.1	120.0	259.0	293.5	550

For a proton incident upon the decay detector, particle identification is possible by plotting the response from ΔE1 vs. (ΔE1 + ΔE2) for energies between 9.2 and 13.5 MeV. For energies between 13.5 MeV and 73.6 MeV, a plot of the response from ΔE1 vs. (ΔE1 + ΔE2 + E-block layer) can be used for particle identification.

Particles with azimuthal angle between 4° and 45° relative to the beam direction will hit the decay detector. Coincident responses from the ΔE1 and ΔE2 layers determine the particle angle with a resolution between 1.8° and 3.8°. The angular resolution is dependent on the location of the pixel formed by overlapping vertical and horizontal layers (FIG. 10). A map of the median angular location of each pixel is shown in FIG. 8.

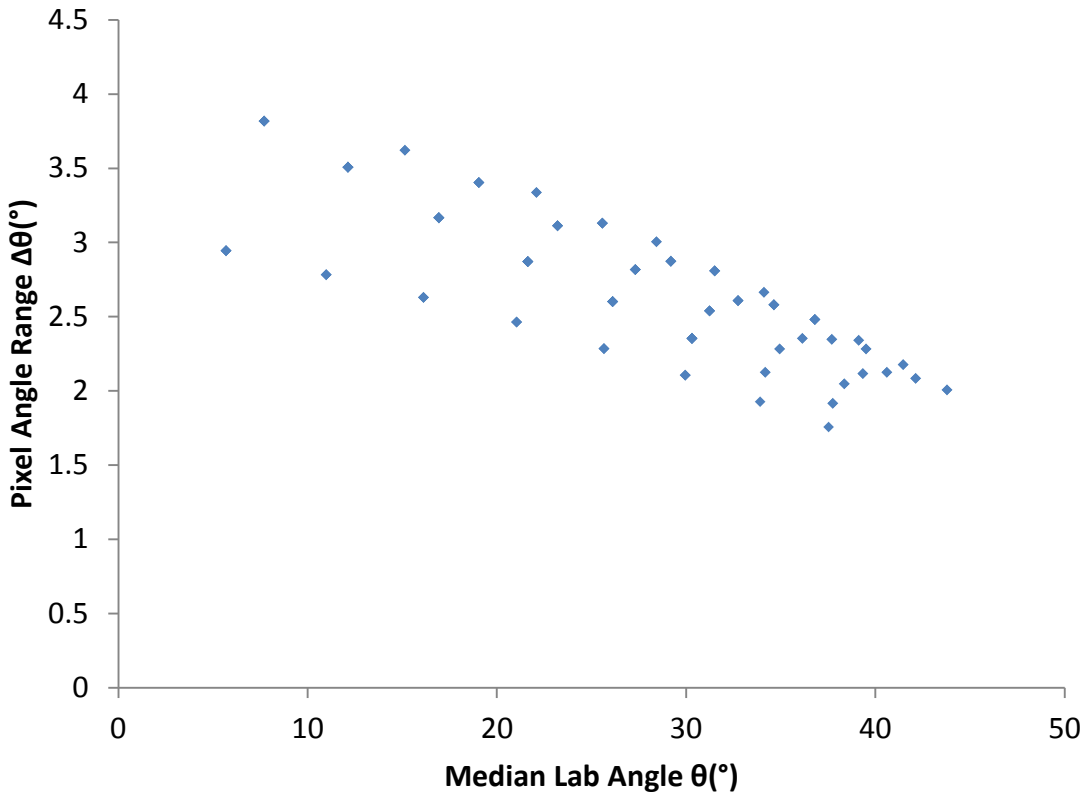

FIG. 10: Plot of pixel angle range vs. pixel median angle. The location on the ΔE1-ΔE2 array of each pixel and corresponding median angle is depicted in FIG. 8.

2.4 Target Chamber Modification

In order to use this detector in the scattering chamber of the MDM, two major modifications were required. The height of the chamber must be increased to accommodate the block scintillators with their light guides, and mounts must be provided for all of the phototubes required.

A 3" high aluminum ring was added to the cylindrical wall of the chamber to provide this extension. The small PMTs needed for the scintillator strips are mounted around the outside of the target chamber on this ring. Plexiglas windows for transmission of photons from the scintillator strips and their optical fiber bundles to the PMTs are fixed to the outside of the ring. Optical grease[7] is applied to the window, and the PMT is pressed against the window and held in place by clamps and a frame attached to the ring. A cylindrical μ-metal magnetic shield[8] fits over the PMT. The preceding can be seen in detail in FIG. 11.

[7] Saint-Gobain, BC-630
[8] Hamamatsu, E989-28

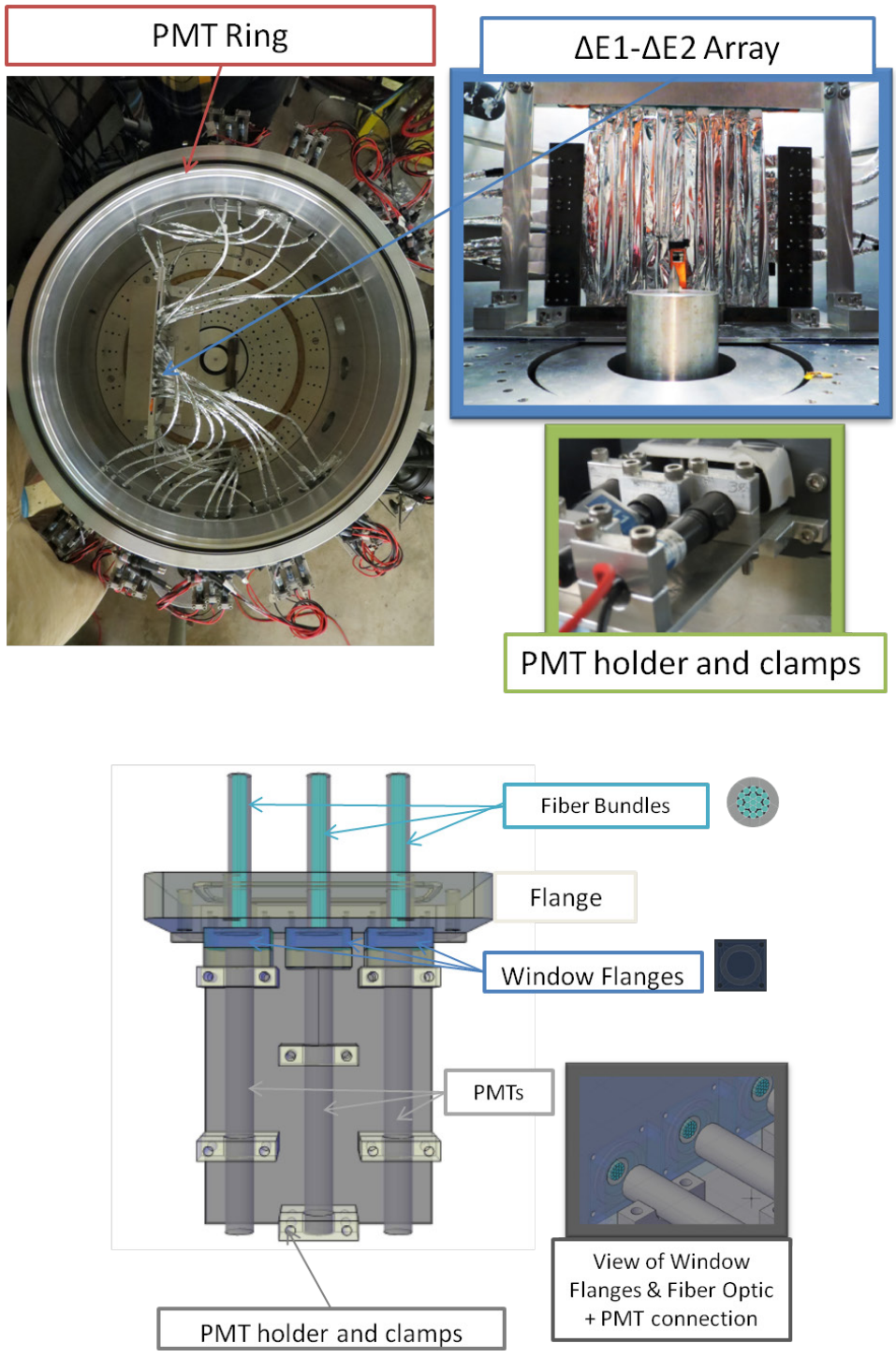

FIG. 11: Top view of the PMT ring and its components. PMTs are clamped onto holders along the outside of the ring. The fiber bundles connected to strip scintillators fit into cylindrical slots and are pressed against clear Plexiglas windows. PMTs are pressed against the opposite side of the window.

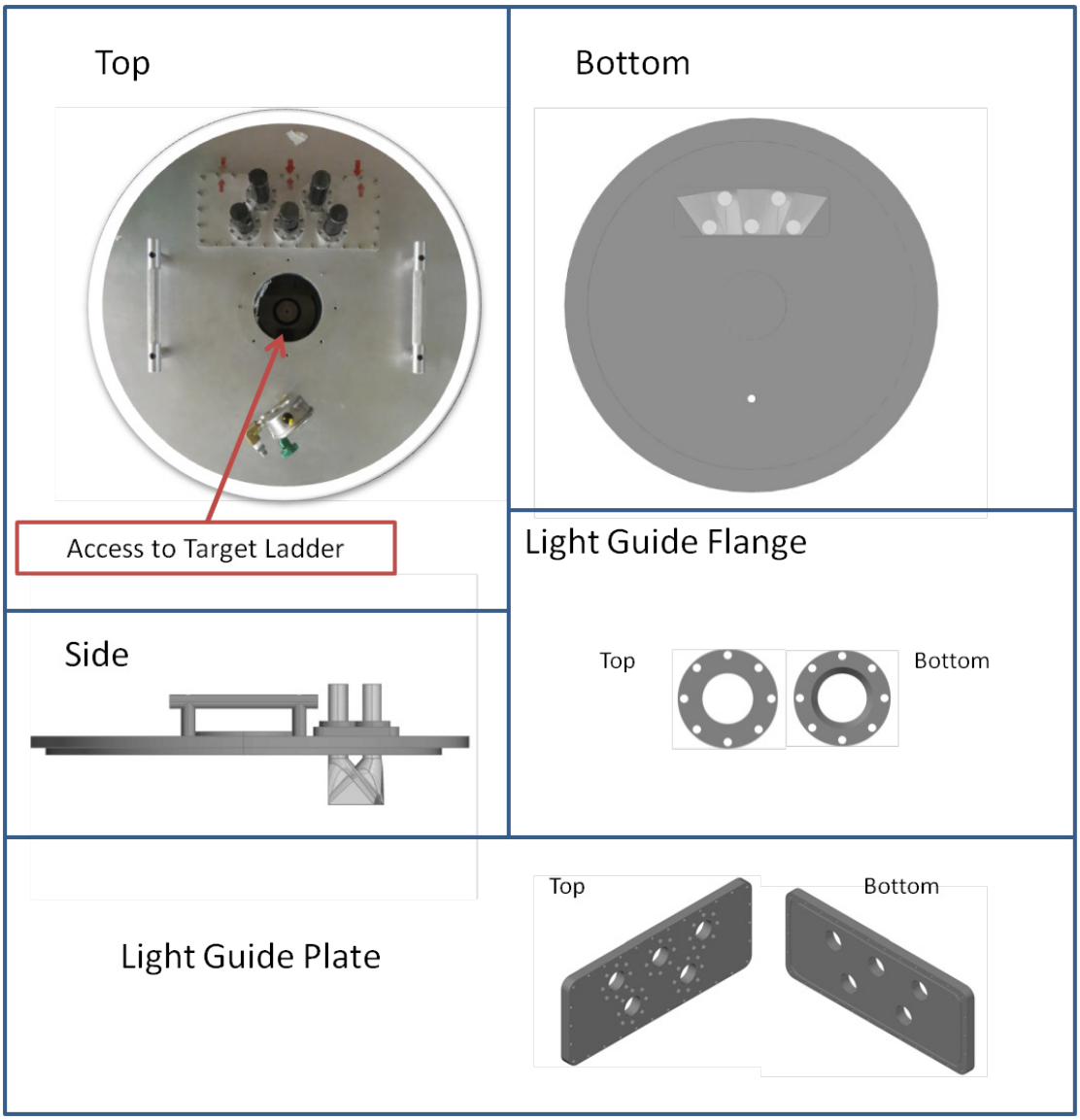

FIG. 12: Views of the target chamber lid and its components. E blocks are fixed to the light guide plate by the light guide flanges.

A new lid (FIG. 12) was made for the chamber with an opening large enough that the scintillator blocks could be removed. The 1" diameter active area PMTs are mounted

to a plate that fits on top of the new lid. Cylindrical Plexiglas light guides of 1" diameter run through the lid and taper out to attach to the scintillator blocks. Aluminum vacuum flanges with a triangular crush groove for the o-ring provide a vacuum seal on the light guides and also hold the light guides in place. In order to accommodate the space requirement for these flanges, the locations of the cylindrical light guides were staggered; this can be seen in the top view from FIG. 12.

2.5 Assembly of Scintillator Strips with Optical Fiber Bundles

Thin strip scintillators are shipped from the manufacturer individually wrapped tightly in thick, clear plastic. To prevent scratching on the surface, they are kept in their wrapper during the process of joining the thin strip with its accompanying optical fiber bundle.

The fiber bundle transports light produced in the scintillator to a 1 cm diameter PMT. The fiber bundle consists of 19 plastic fibers, 1 mm in diameter. The fibers were ordered pre-cut to 50 cm length. On one end, the fibers are shaped into a rectangular form in order to mate with the 1 mm x 1 cm edge of the scintillator strip. In order to maximize light transmission at this end, the fibers are arranged as in FIG. 13, giving the rectangular edge dimensions of 2 mm x 1 cm. The rectangular end is made with optical cement poured into a silicone rubber form with a 2 mm x 1 cm x 1 cm slot. The fibers are pushed into the slot so that they are encased in optical cement while the cement hardens. The rectangular end is then ground down to make it flat relative to the scintillator strip edge. It is then sanded and polished to an optical finish.

The cylindrical end (FIG. 13) is formed by filling a Plexiglas sleeve with optical cement. The fibers are then pushed through the sleeve before the cement completely hardens. After the cement has hardened, the end is ground down flat and then sanded and polished to an optical finish.

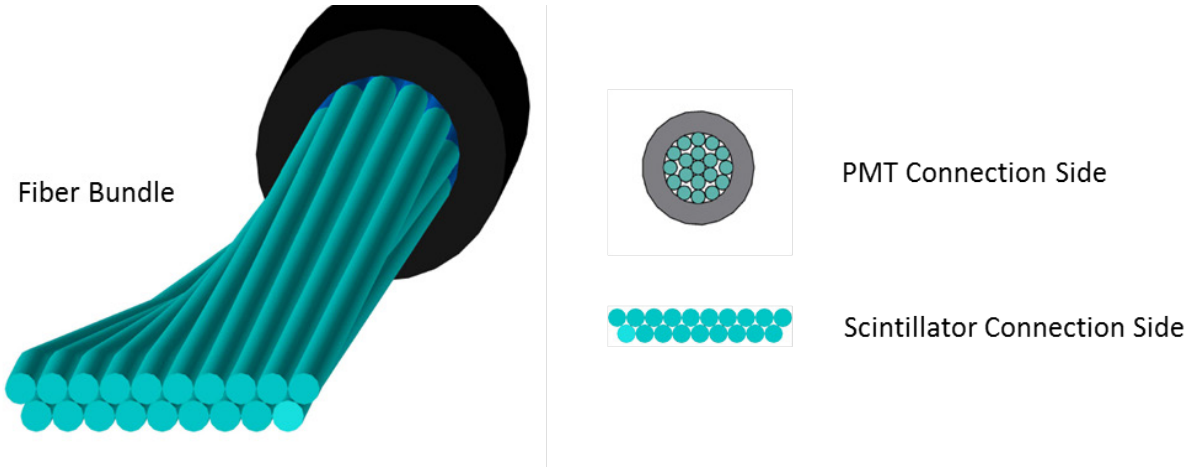

FIG. 13: Fiber bundle construction. This is a schematic of the rectangular and cylindrical ends of a typical fiber bundle.

A casing covering the joint between the thin strip scintillator and its fiber bundle is composed of 4 pieces of thin Plexiglas (FIG. 14). The Plexiglas is attached to the fiber bundle using super glue. This results in a small cavity large enough to snugly fit over the outer dimension of the scintillator (FIG. 14, lower left). The cavity is filled with optical cement. The scintillator is inserted into the cavity and then held in place with small

clamps while the cement hardens. This method ensures proper alignment of the

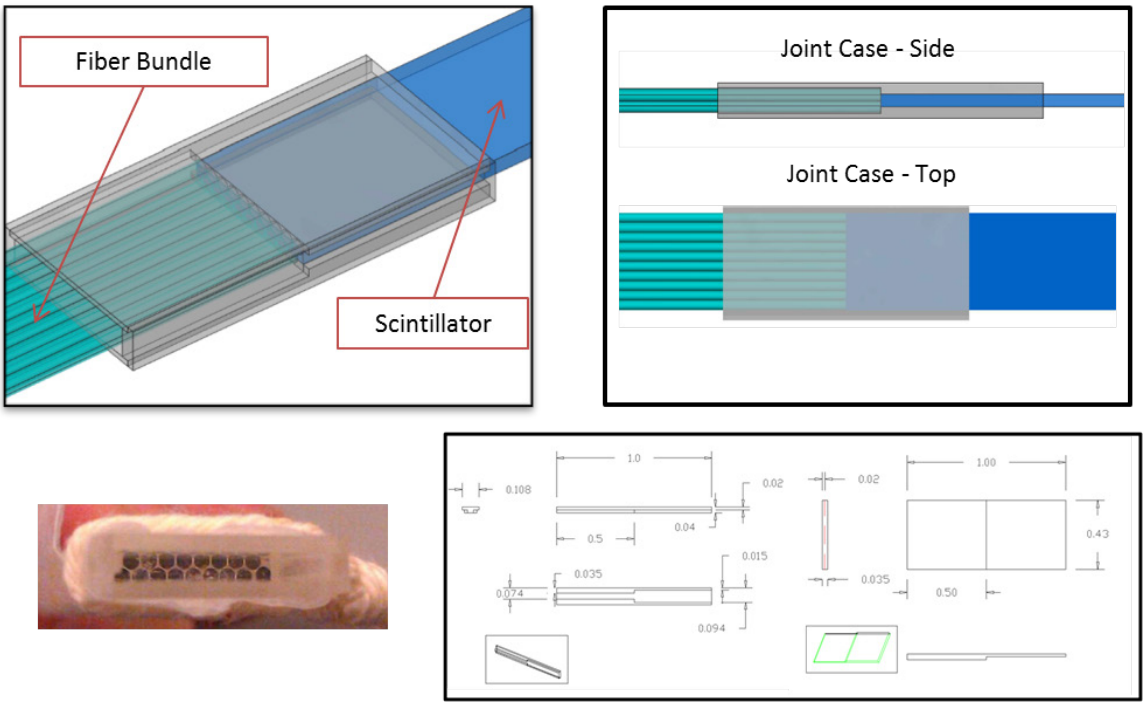

FIG. 14: The optical connection between fiber bundle and scintillator strip. Two of each piece depicted in the lower right hand corner drawing are used to make the joint case. A photo of the step prior to filling the joint case cavity with optical cement and inserting the plastic scintillator is shown in the lower left. Proper alignment of a finished optical connection is shown on top.

scintillator strip with the fiber bundle. The casing covering the joint is adequately strong and uniform in shape, such that the strip and bundle may be held in place and properly aligned onto the detector frame.

An aluminized Mylar sleeve was constructed to fit snugly along the length of the thin strip scintillator. Consisting of two layers of 2 μm thick aluminized Mylar, the sleeve adequately blocks outside light and improves light transmission of optical photons.

The sleeve (FIG. 15) is advantageous because it can be quickly applied or

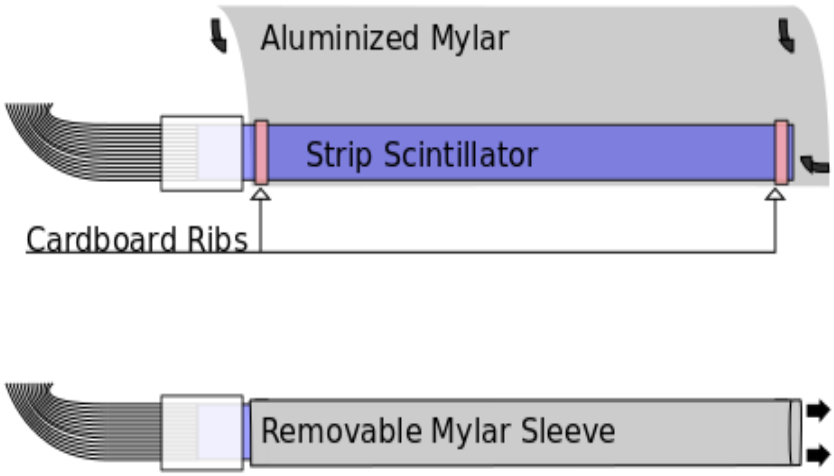

FIG. 15: Construction of the aluminized Mylar sleeve for thin strip scintillators.

removed with a minimum amount of handling of the scintillator itself, which is beneficial because excessive, rough handling of the scintillators results in surface cracking (crazing) and reduced efficiency of light transmission. First, a thin sheet of

cardboard is formed to wrap over the scintillator once. It is closed by applying double-sided tape. This cardboard sleeve is then cut into thin pieces and wrapped in double-sided tape along its outside. Using a thin piece of plastic with the dimension of the thin strip scintillator as a jig, the thin cardboard pieces are slipped onto the ends. The aluminized Mylar is then wrapped over this twice and is closed at one end with another application of double sided tape.

2.6 Block Scintillators

The block scintillators are coupled with light guides that taper from the shape of the block to a 1" diameter circle. These light guides are then coupled with cylindrical light guides that pass through the target lid light guide plate to mate with 1" diameter PMTs. The flanges that hold these light guides to the top of the target chamber lid are too large for the cylindrical light guides to be centered over the block scintillators. For this reason, the cylindrical light guide positions are staggered, as seen in FIG. 12. The shape of each light guide was created by taking the intersecting volumes of 2 shapes. The first is a 2.5 in. tall extrusion of the block scintillator shape, as is shown in FIG. 16.

The other is an eccentric cone whose base is a circle with the minimum diameter required to circumscribe the block scintillator shape (in the example shown in FIG. 16, this diameter is 3.53”), the center of which is at an angle with respect to the center of the

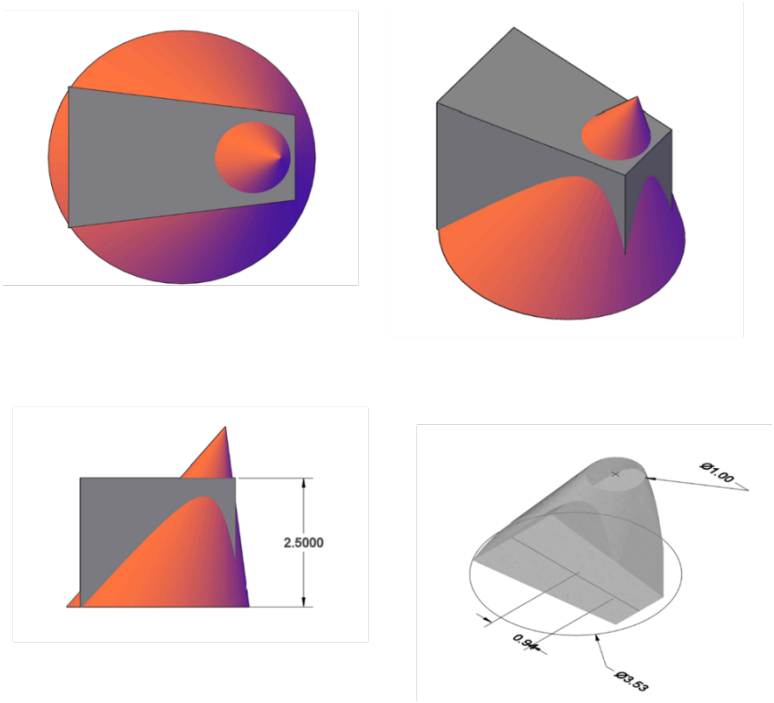

FIG. 16: Design for the E3 block light guide. The geometry of the light guide comes from the intersection of a 2.5” tall extrusion of the scintillator shape with an eccentric cone.

1 in. diameter base of the cylindrical light guide (in the projection of the small radius circle onto the base, the center of the small circle is offset from the center of the base circle by 0.94”).

The scintillator, odd-shaped light guide, and cylindrical light guide are joined by optical cement.

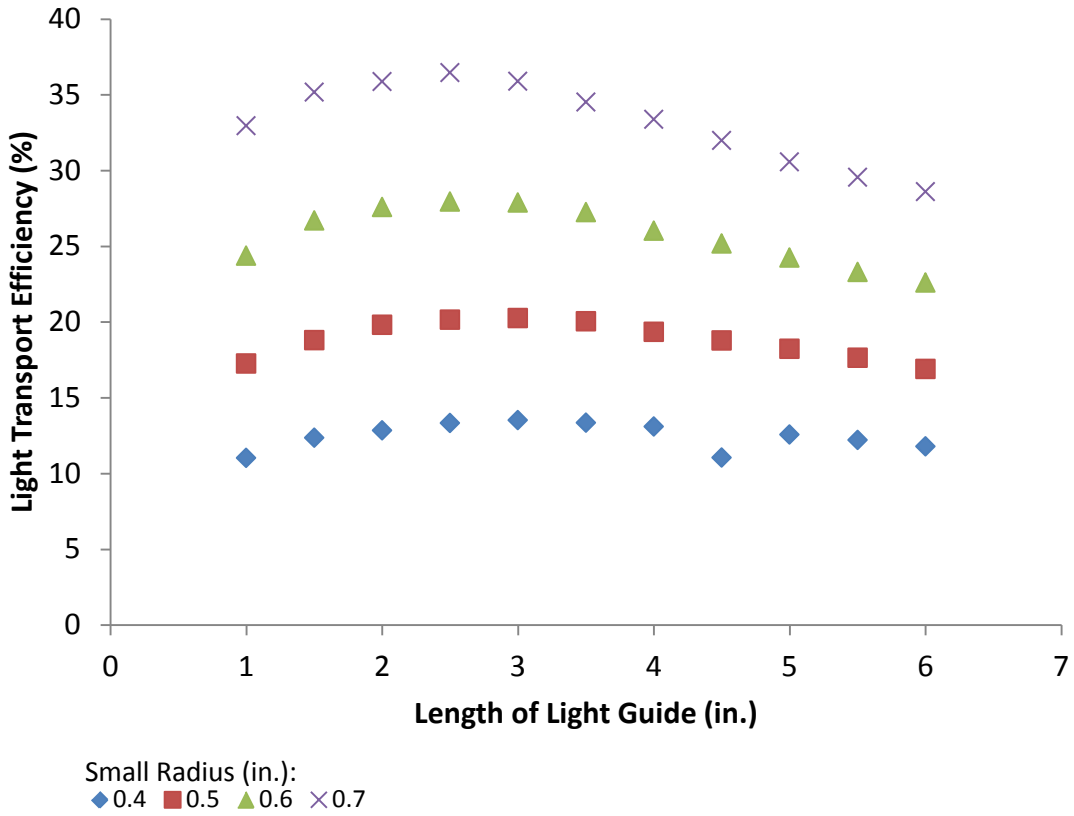

FIG. 17: Plot of the light transport efficiency vs. the length of the eccentric cone light guide for different radii of the small circle, obtained from the GuideIt simulation.

The height of the eccentric cone was optimized using results from the light transmission simulation GuideIt (FIG. 17). The light transport efficiency was calculated

for light guides of various lengths and with small circles of different radii. For each value of the small radius, the light transmission efficiency is optimum when the light guide length is 2.5”. The small radius was constrained by the dimension of the PMTs (1”).

The side of each block scintillator which touches the ΔE2 layer is covered in 1 layer of aluminized Mylar (FIG. 18, right). Two layers of aluminized Mylar are on the

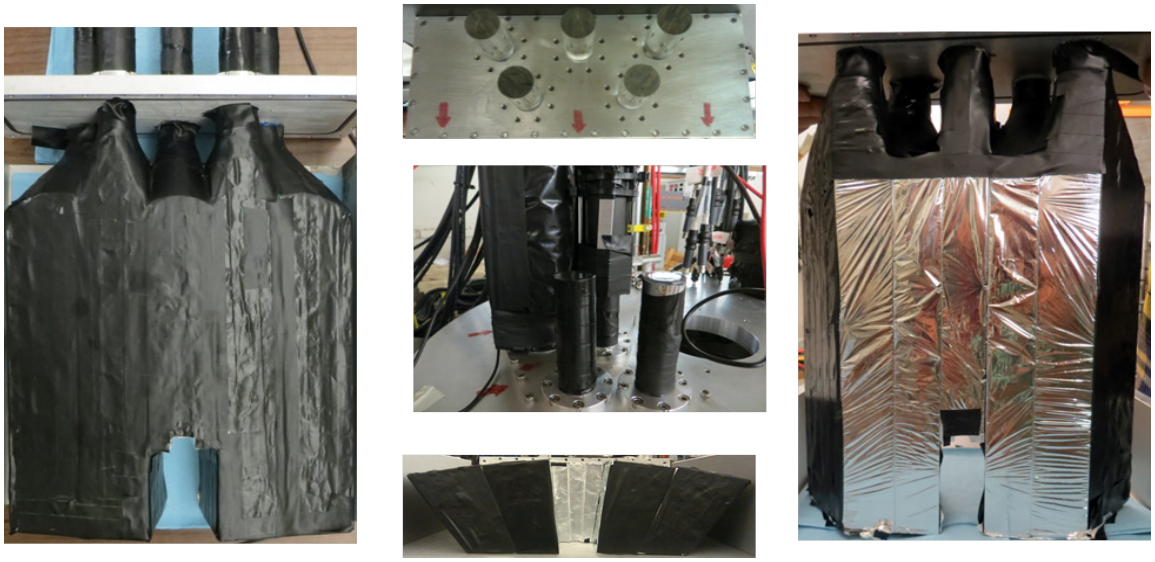

FIG. 18: Photos of wrapped and assembled block scintillators and light guides

sides which touch neighboring block scintillators. The remaining sides are covered in aluminized Mylar as a first layer in order to make a good reflective surface. Several additional layers of aluminum foil and black electrical tape were used on the remaining sides in order to block ambient light (FIG. 18).

3. LIGHT RESPONSE OF PLASTIC SCINTILLATORS

3.1 Introduction

A scintillator is a material which has a fluorescent response when exposed to ionizing radiation. The initial scintillation is due to the excitation and subsequent de-excitation of atomic electrons within the material. The scintillating material is doped with a fluor which shifts scintillation light into the visible part of the spectrum (typically in the green to blue wavelengths). An atomic electron in the fluor enters into an excited state following absorption of a photon. Non-radiative processes may be involved in the relaxation back to the ground state, for example some excitation energy may be lost as heat, which allows for emission of the longer wavelength or lower energy photon. Generally, the light response is linearly proportional to the incident ion energy. However, when the incident ion energy is low (the energy region $E/A < 15$MeV/amu in the case of plastic scintillators), the response is non-linear as a result of quenching effects [8]. In this type of detector, the light response is converted into a current by a photomultiplier tube (PMT).

Stopping range tables [7] were used in order to make estimates of the ion energy loss in the different layers of the decay detector for different incident ion energies and ion types of interest (proton, α, and ^{6}Li). Accurate prediction of the stopping power of ions at different energies is an important factor in calculating the light response by plastic scintillators.

The Energy Deposition by Secondary Electrons (EDSE) model [9] was used for making estimates of the light response. This model is advantageous for calibration

purposes because its most significant parameter, the quenching energy density ρ_q, is dependent on the scintillator material, rather than the charge of the incident ion.

An important characteristic of scintillators is the attenuation length λ of the light response, which is defined as the length for which the probability that a photon is not absorbed is 1/e. Due to the long and thin geometry of the strip scintillators (Saint Gobain BC408, dimensions 1mm x 1cm x 18cm), the attenuation length of the light response as quoted by Saint-Gobain (λ=210 cm) [10] is unreliable because it is only valid for a bulk scintillator where the maximum distance from the connected PMT is small relative to the scintillator's height and thickness. A simulation of optical photon transport in the strip scintillators was used to make a more accurate estimate of the attenuation. In Chapter 4, this estimate is compared to measurement.

3.2 Stopping Range of Ions in Materials (SRIM)

SRIM [7] is a computer program that calculates the stopping power dE/dx for an incident ion on a target. The incident ion loses energy in the target material via nuclear (elastic) and electronic (inelastic) collisions.

The nuclear stopping power is due to interaction of the incident ion with a screened Coulomb potential.

$$V(r) = \frac{1}{4\pi\epsilon_0}\frac{Z_1 Z_2 e^2}{r}\,\phi\left(\frac{r}{a}\right) \tag{15}$$

This treatment is similar to that of the Lindhard-Schiff-Schiott (LSS) theory [11], with the exception that parameters of the screening function ϕ(r/a) in the SRIM calculation are found by fit to experimental data rather than derived from first principle.

$$a = \frac{0.8854 a_0}{Z_1^{0.23} + Z_2^{0.23}} \tag{16}$$

$$\phi(r/a) = 0.1818\, e^{-3.2r/a} + 0.5099 e^{0.9423r/a} + 0.2802 e^{-4029r/a} + 0.02817 e^{0.2416r/a} \tag{17}$$

In the equation for the screening function, a_0 is the Bohr radius, and Z_1 and Z_2 are the atomic numbers of the incident ion and material. At high energy, the nuclear stopping power simplifies to the case of Rutherford scattering. Interpolation methods are used to bridge the gap between energy regimes. For energies above 1MeV/amu, the nuclear contribution to the total stopping power is negligible.

Above 1 MeV/amu, the electronic stopping power can be calculated with the relativistic Bethe-Bloch formula EQ. (18), which is a quantum mechanical formulation of the energy loss using the first Born approximation.

$$-\frac{dE}{dx} = \frac{4\pi}{m_e c^2} \frac{nz^2}{\beta^2} \left(\frac{e^2}{4\pi\epsilon_0} \right)^2 \left[\ln\left(\frac{2 m_e c^2 \beta^2}{I(1-\beta^2)} \right) - \beta^2 \right] \tag{18}$$

In the formula, I is the mean ionization potential, β is the relative velocity v/c, m_e is the electron mass, e is the electron charge, ϵ_0 is the electric permittivity, and n is the density of target atoms per unit volume.

At lower energies, the electronic stopping power is determined using functions fitted to experimental data. When the energy is below 25 keV/amu, the stopping power is of the form (where A_i are arbitrary parameters that fit the data):

$$\frac{dE}{dx}_{Low} = A_1 E^{A_2} + A_3 E^{A_4} \tag{19}$$

When the energy is above 200 keV/amu but below the region where the Bethe-Bloch formula is applicable, the stopping power is of the form:

$$\frac{dE}{dx}_{High} = \frac{A_5 \ln\left(\frac{A_6}{E} + A_7 E\right)}{E^{A_8}} \tag{20}$$

For the region between 25 and 200 keV/amu, the stopping power is calculated using:

$$\frac{1}{dE/dx_{Int}} = \frac{1}{dE/dx_{Low}} + \frac{1}{dE/dx_{High}} \tag{21}$$

The scintillating material [10] used in the decay detector consists of 94% Polyvinyltoluene ($C_{27}H_{30}$) as a base with 6% Anthracene ($C_{14}H_{10}$) as a fluor, at a density of 1.032 g/cc. Tables of the stopping power (dE/dx [MeV/mm]), range, and range straggling for different incident ions over the appropriate energy range were produced from Eqs (18) - (21)) and used to estimate the light response of the various scintillator elements in the decay detector.

To calculate energy deposited into the 1 mm thick strips of scintillator, a simple numerical integration technique was used. From the calculated dE/dx and the known thickness of the scintillator material (y), an estimate of the energy deposited is

$$E_{loss} = \sum_{i=1}^{n} \left(\frac{y}{n}\right)\left(\frac{dE}{dx_i}\right) \tag{22}$$

The calculation is restricted to the range of energies incident upon the first layer such that the ion is stopped in either the second or third layer. The remaining energy after the ion passes through the first two strip layers is deposited into the E-Block. The energy

deposited into each layer for different incident ion energies and types is shown in FIG. 19.

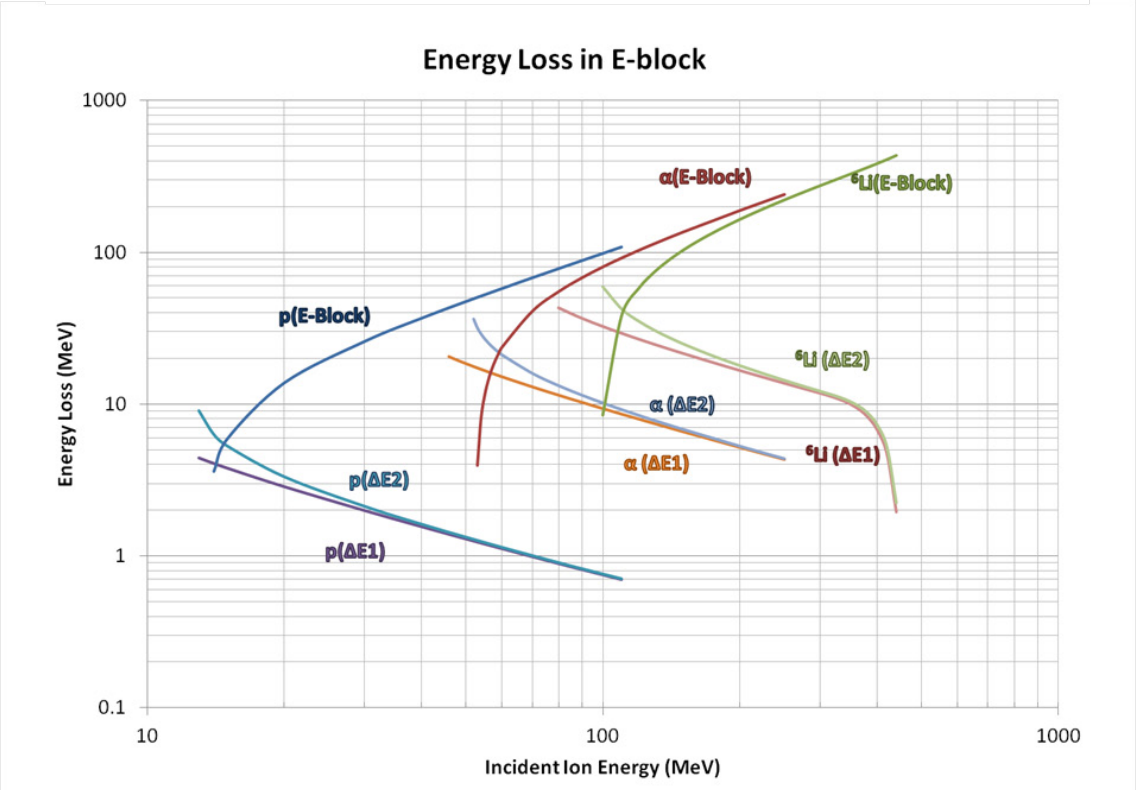

FIG. 19: Plot of ion energy loss in each of the three scintillator layers vs. the incident ion energy prior to entering the detector. For protons, α particles, and ^{6}Li ions, this is shown for incident energies such that the ion is stopped in either the second layer (ΔE2) or the third layer (E-Block).

3.3 Models for Scintillator Light Response

In the Birks model [8], the specific light response (dL/dx) due to ions passing through the scintillator is given by:

$$\frac{dL}{dx} = \frac{A\frac{dE}{dx}}{1 + kB\frac{dE}{dx}} \tag{23}$$

The number of energy carriers produced due to passage of an ion in the scintillator is proportional to the energy loss (A dE/dx) of the incident ion. The observed non-linearity in the light response is due to energy carriers that are captured by damaged or ionized molecules in the scintillator; this effect is referred to as quenching. The number of damaged molecules is proportional to the energy loss (B dE/dx), because a local concentration of damaged molecules is produced by the passage of the ion through the scintillator material. The parameter k is the probability that an energy carrier is captured by a damaged molecule. The parameters (A and kB) are determined by experiment and vary depending on the incident particle and scintillator material type.

The Energy Deposited by Secondary Electrons (EDSE) model provides a useful tool for calibrating the scintillator response and extrapolating the ion energy deposited because the model parameters are dependent on the scintillating material used and independent of the charge of the incident ion.

An algebraic expression for the light output (dL/dx) is derived by making reasonable approximations of the physical processes involved in the conversion of deposited ion energy into optical photons. In the scintillator, ionizing radiation is converted into light via the creation of energy carriers, dN/dx (either particle-hole pairs

or excited molecular structures). A full description of the model can be found in the Michaelian paper [9] and the references therein.

The basis for the EDSE model is that non-linearities in the light response are due to a high density of energy carriers around the ion track through the material. The density of energy carriers is assumed to be proportional to the energy distribution of scattered electrons in the material. This energy density distribution takes the form:

$$\rho(r) = N_A \frac{Z_{eff}}{A_{eff}} \rho_m \frac{e^4}{m_e} \frac{z^{*2}}{V^2} \left(1 - \frac{r}{R_{max}}\right)^{d+\frac{1}{n}} \tag{24}$$

where N_A is Avogadro's number, Z_{eff} and A_{eff} are the mean charge and mass of the material, ρ_m is the material density in g/cm^3, e and m_e is the charge and mass of the electron, V is the ion velocity, and z* is the effective charge of the incident ion. The exponent, d+1/n, is unique to the material and is approximately (.752) for the plastic scintillator used in the decay detector. The constant *d* comes from the theory by Everhart [12] describing the range of electrons in matter and has been determined experimentally to be 0.045 Z_{eff}. The constant *n* comes from the equation for the electron range-energy relation (EQ. (25)). The Kanaya and Okayama [13] derivation of the electron range-energy relation is based on the electron-atom interaction described by Lindhard [11] and fits experimental data. In their result, *n* = 5/3 and a is given by EQ.(26). R_{max} is the range of an electron with the maximum kinetic energy (T) transfer from the incident ion.

$$R = a\, T^n \tag{25}$$

$$a = \frac{5.025 \times 10^{-12} A_{eff}}{0.182\, \rho Z_{eff}^{\frac{8}{9}}} \tag{26}$$

Inefficiency in the light conversion is introduced via the quenching energy density ρ_q. For values of $\rho(r) > \rho_q$, no additional energy carriers are created. The associated quenching radius r_q is the value of r such that $\rho(r) = \rho_q$. Plots of $\rho(r)$ and r_q for various ion types at the same incident ion energy are shown in FIG. 20.

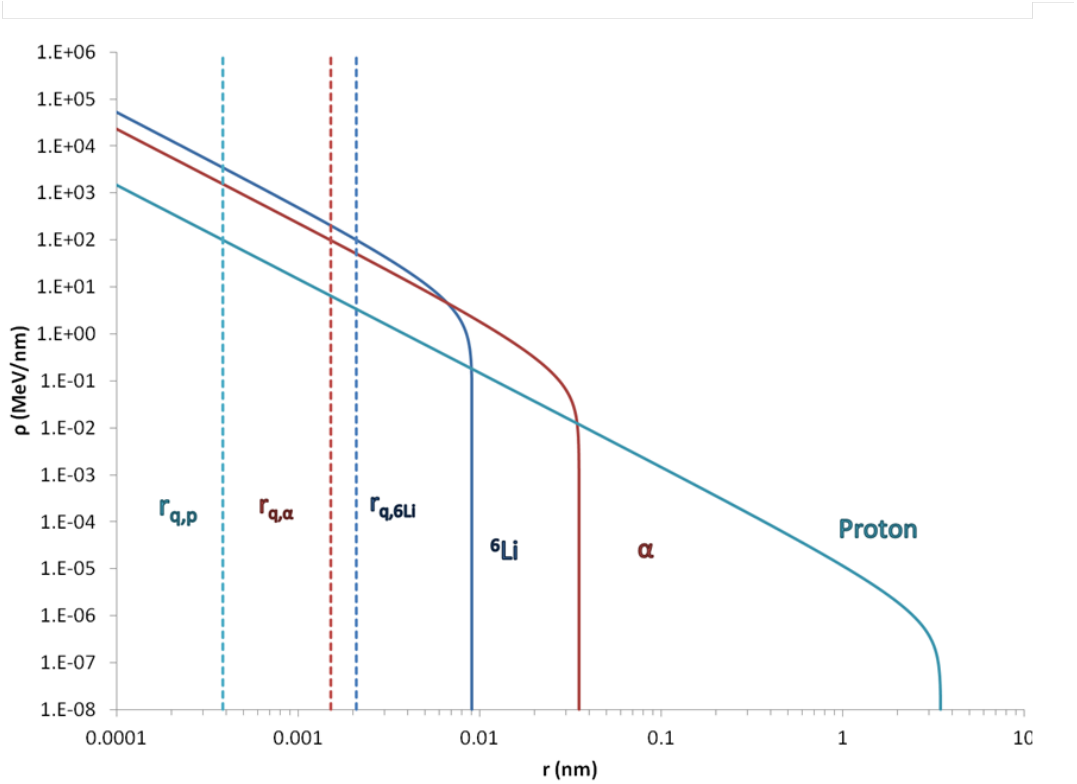

FIG. 20: Plot of the energy density of secondary electrons with respect to radial distance, r, from the ion track for protons, α particles, and ^{6}Li ions. The ion energy is 9 MeV. The dashed line shows the position of the quenching radius (r_q), which is the value of r such that $\rho(r) = \rho_q$, the quenching energy density (99.7 MeV/nm).

The number of energy carriers around a segment of the ion track (dN/dx) is then calculated by radial integration of ρ(r):

$$\frac{dN}{dx} = K\left(\pi r_q^2 \rho_q\right) + 2\pi \int_{r_q}^{R_{max}} \rho(r) r dr \tag{27}$$

A reasonable approximation for the integral of the radial energy density can be done analytically for $d + \frac{1}{n} = \frac{3}{4}$. For $\mathcal{R} \equiv 1 - \frac{r_q}{R_{max}}$ the result is as follows:

$$\int_{\mathrm{r}}^{\mathrm{R}} \rho(\mathrm{r}) \mathrm{r} \mathrm{dr} = \frac{\mathrm{N_A Z_{eff}}}{\mathrm{A_{eff}}} \rho_{\mathrm{m}} \frac{\mathrm{e}^4}{\mathrm{m_e}} \frac{\mathrm{z}^{*2}}{\mathrm{V}^2} \left[-\ln\left(\frac{1 - \mathcal{R}^{\frac{1}{4}}}{1 + \mathcal{R}^{\frac{1}{4}}}\right) - 2\arctan \mathcal{R}^{\frac{1}{4}} - \frac{5}{6}\mathcal{R}^{\frac{3}{4}} \right. \tag{28}$$

The number of energy carriers is then related to luminescence by EQ. (29), where F is the inefficiency of the conversion of energy carrier to light and A is the number of states that can fluoresce without quenching.

Finally, numerical integration of dL/dx over the ion path, x, gives the total light output.

$$\frac{\mathrm{dL}}{\mathrm{dx}} = \mathrm{C} \frac{\mathrm{dN}}{\mathrm{dx}} \left(1 - \frac{\mathrm{F} \frac{\mathrm{dN}}{\mathrm{dx}}}{\mathrm{A} + \frac{\mathrm{dN}}{\mathrm{dx}}} \right) \tag{29}$$

A fit to published experimental data [14] is shown in FIG. 21. Using the parameters obtained from this fit, the responses predicted for each of the three scintillator layers are shown in FIG. 22 and FIG. 23.

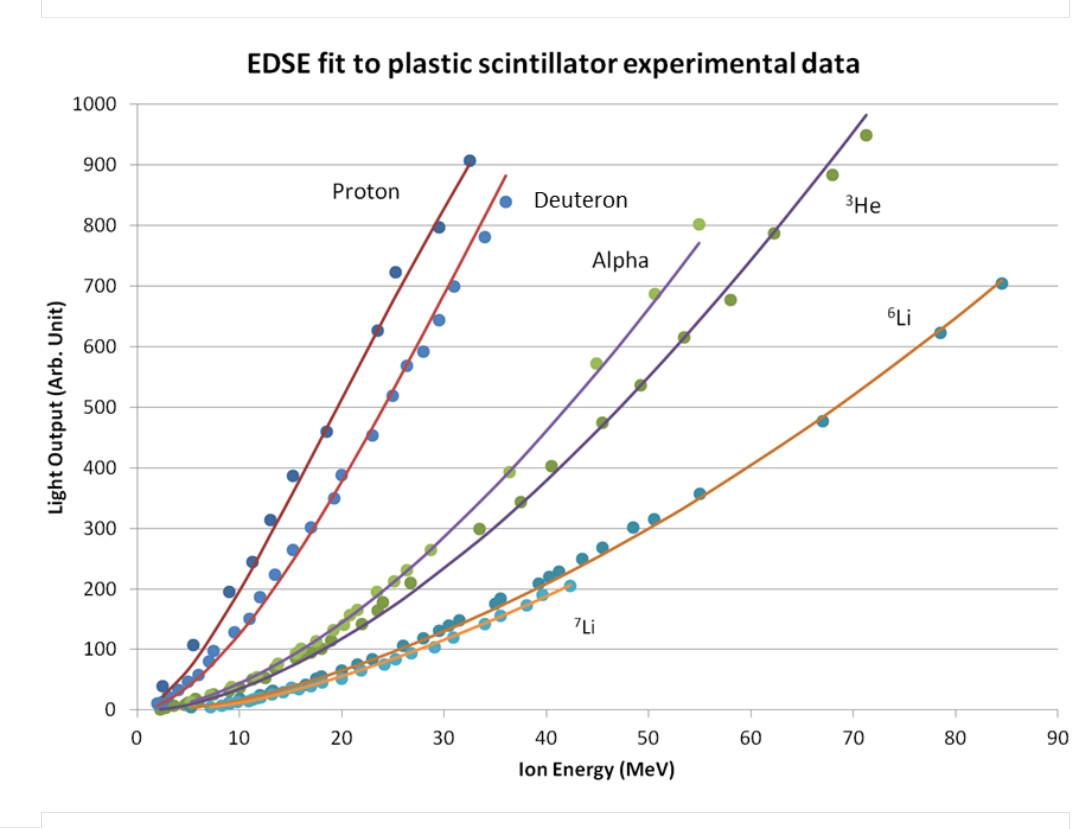

FIG. 21: Fit to published experimental data of the light response of plastic scintillator [14]. The parameters obtained by chi-square fits have the values ρ_q = 99.7 MeV/nm, F = .998, A = 1x10^{-4}, C_{proton} = 1.14, C_{α} = 1.96, and C_{6Li} = 2.90.

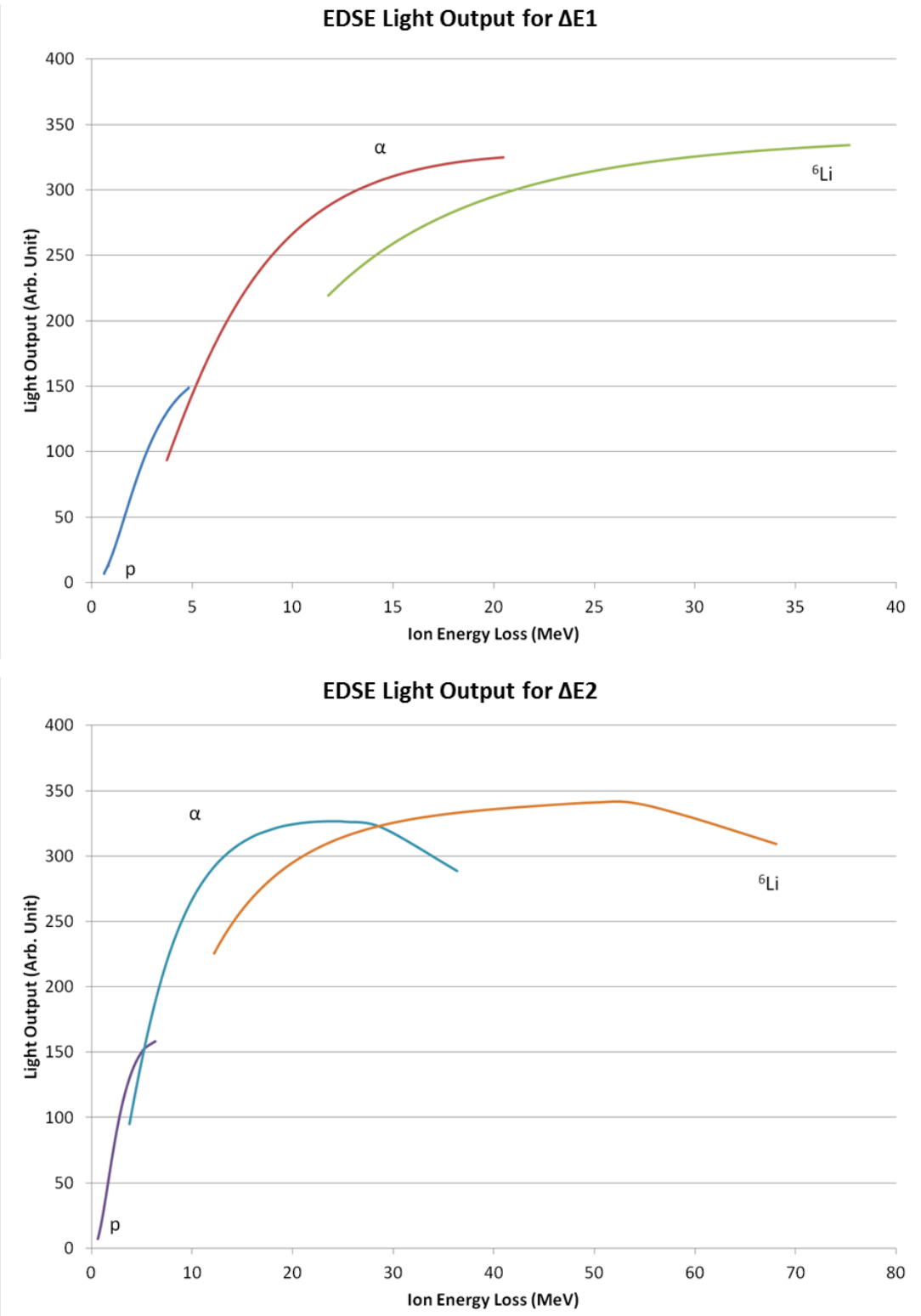

FIG. 22: Light response of a strip detector in the first and second layer of the decay detector as a function of the energy deposited in the strip by protons, α particles and ^{6}Li ions which stop in either ΔE2 or the E-Block.

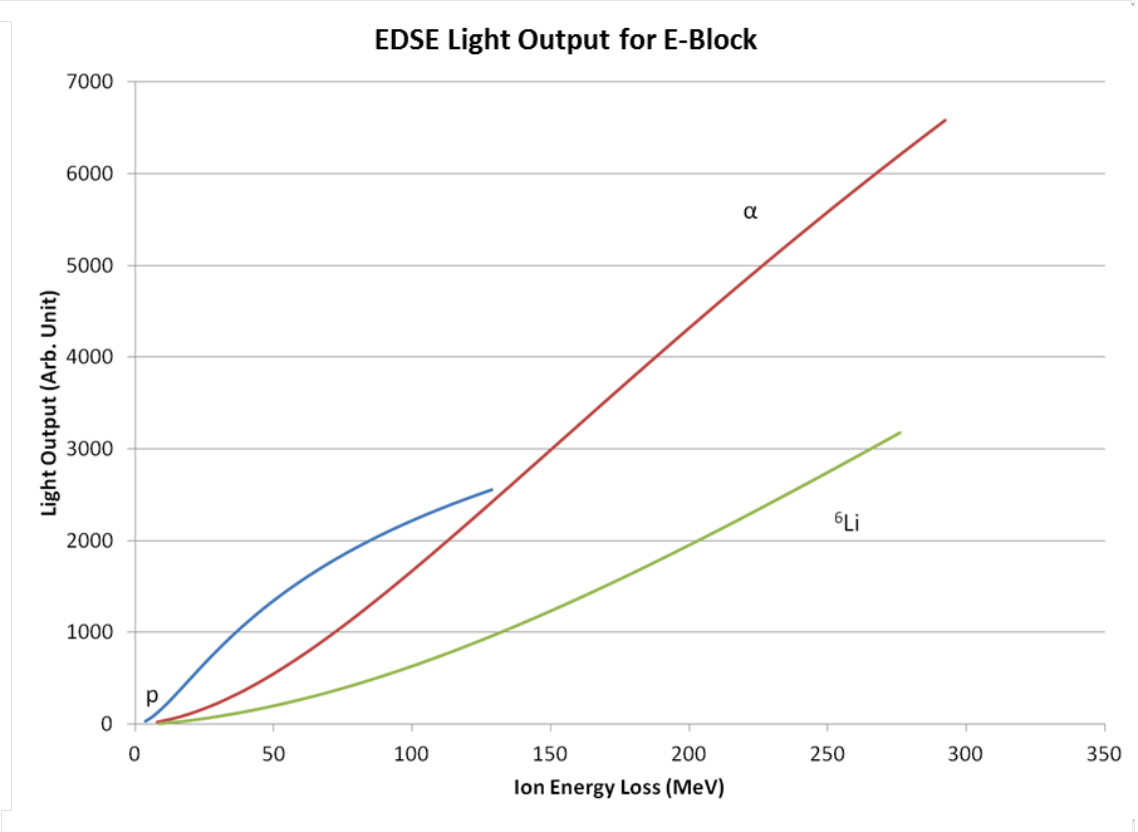

FIG. 23: Light response of a block in the third layer of the decay detector as a function of the energy deposited in the strip by protons, α particles and ^{6}Li which stops in the E-Block.

3.4 Light Attenuation in Scintillator Strips

Of particular concern with the scintillator strips is the reduction of the light response due to photons which leave the scintillator when they strike a surface boundary of the material before entering the light guide. This was estimated by modeling the strip as a 3D rectangular volume (1 mm x 1 cm x 18 cm) in which photons are emitted randomly in position and momentum with an overall uniform distribution. The fraction of the emitted photons that reach the fiber optic cable is then obtained as a function of position along the strip.

When the photon strikes a boundary, if the angle of the photon trajectory relative to normal is greater than or equal to the critical angle (refractive index of 1.58) [10], then the photon reflects off the surface and remains inside the scintillator. For angles less than the critical angle, the reflection and transmission probabilities are calculated and then used to determine whether or not the photon remains inside the scintillator. The efficiency of the scintillator is determined by dividing the number of photons that arrive at the fiber optic end by the total number of photons generated. The efficiency is plotted with respect to initial position of the randomly generated photon from the end of the scintillator connected to the fiber optic bundle in FIG. 24. The data were fit with a sum of two exponential decay curves ($y=a_1e^{-x/\lambda 1}+a_2e^{-x/\lambda 2}$). The first curve is the transmission behavior for photons with angles less than the critical angle when incident on a surface. The attenuation length ($\lambda_1 = 1.8$ cm) for this mode of transmission is very short relative to the length of the scintillator. The second curve is the transmission behavior for photons that are not incident on a surface or have angles greater than or equal to the

critical angle when incident on a surface. The attenuation length (λ_2 = 104.3 cm) for this mode is much longer.

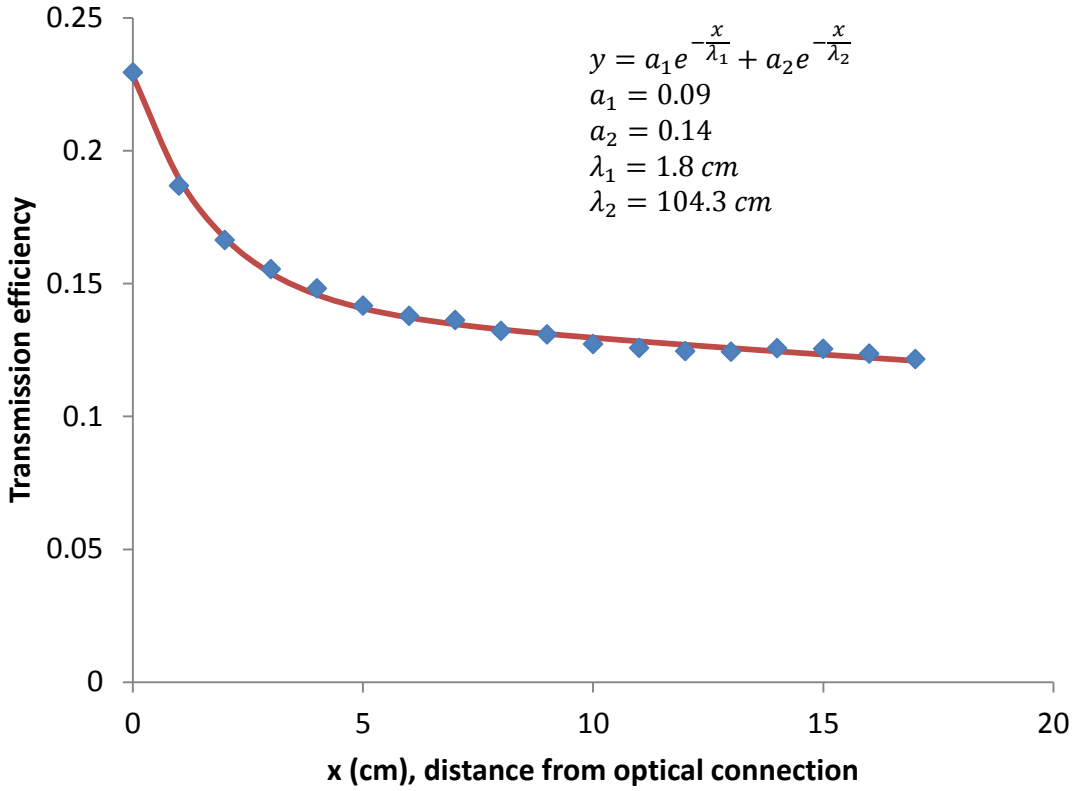

FIG. 24: Simulation result for the transmission efficiency of optical photons in a thin, strip scintillator (1cm x 1mm x 18 cm) with respect to the initial distance of the photon from the scintillator connection with its PMT.

4. TEST RUN AND ANALYSIS RESULTS

4.1 Introduction

A test run of the completed decay detector was done using a beam of 30 MeV protons on a ^{12}C target. Data collection was triggered by signals from the strip layer ΔE2. Since real proton events must also have a signal in ΔE1, only events with both ΔE1 and ΔE2 signals were analyzed.

The ΔE2-E 2D-spectra (FIG. 25) show three distinct peaks due to protons of

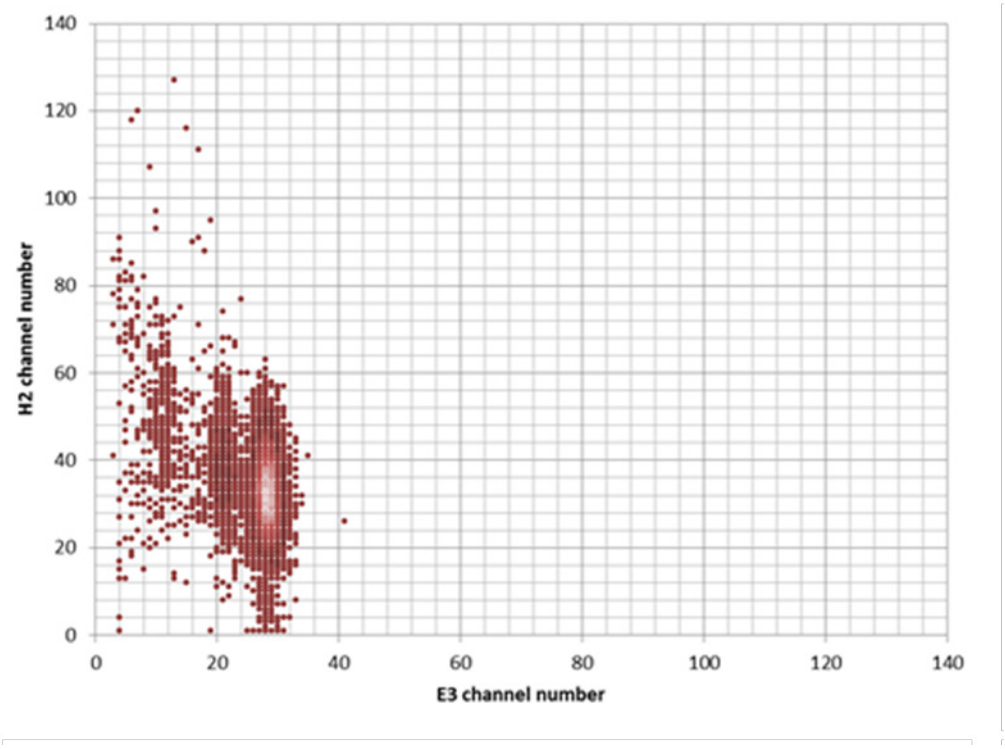

FIG. 25: Example ΔE2-E 2D-spectrum: Lighter shades of red are used to indicate greater numbers of counts.

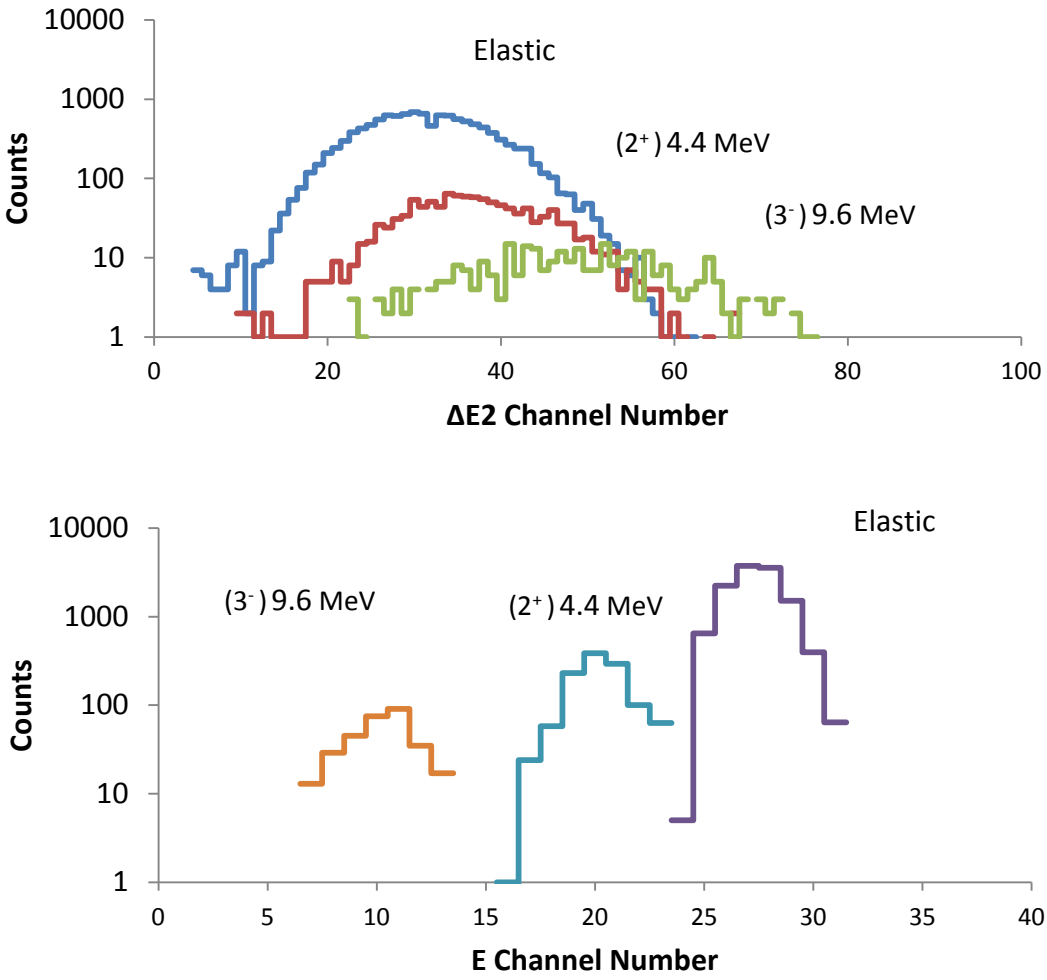

FIG. 26: Example 1D-spectra resulting from gates on peaks in the ΔE2-E 2D-spectra (FIG. 25).

different energies from elastic scattering and inelastic scattering exciting the 4.4 MeV (2+) and 9.6 MeV (3-) levels in ^{12}C [15]. To confirm this, ΔE2 and E 1D-spectra (FIG. 26) corresponding to each of the three peaks visible in the 2D-spectra were produced. Each peak in the resulting 1D-spectrum was fit with a Gaussian. The average peak position agrees with the expected light response of the ΔE2 layer and E-Block (TABLE

IV and TABLE V). The expected light response was calculated by first solving for the energies (corresponding to the spread in the azimuthal angle relative to the beam direction within the overlapping ΔE2-E area) of the incident proton on ΔE1 using relativistic kinematics. The energy deposited in each layer was found by using the SRIM tables, and the EDSE model was used to calculate the expected light response.

TABLE IV: Comparison of the light response in block E3 in coincidence with horizontal strip H2 at 3 different proton energies: The decay detector area corresponding to the overlap of E3 and H2 is at an azimuthal angle relative to the beam direction of 33±2°. The uncertainty in the energy incident on ΔE1 is due to the uncertainty of the proton angle. The energy deposited in E3 is found by consulting the SRIM tables [7].

	Energy incident on ΔE1 (MeV)	Energy Deposited in E3 (MeV)	Exp. L.O. E3 (Ch. Number)	Relative Exp. L.O. E3	EDSE L.O. E3 (Arb. Unit)	Relative EDSE L.O. E3
Elastic	29±1	25±1	28 ± 2	1.00	660±4	1.00
2^+	24±1	20±1	21.1 ± 0.1	0.8±0.1	498±5	0.8±0.1
3^-	19±1	13±1	12 ± 3.0	0.4±0.1	279±4	0.4±0.1

TABLE V: Comparison of the light response in strip H2 in coincidence with E-block E3 at 3 different proton energies: The decay detector area corresponding to the overlap of E3 and H2 is at an azimuthal angle relative to the beam direction of 33±2°. The uncertainty in the energy incident on ΔE1 is due to the uncertainty of the proton angle. The energy deposited in ΔE2 is found by consulting the SRIM tables [7].

	Energy Deposited in ΔE2 MeV	Exp. L.O. H2 (Ch. Number)	Relative Exp. L.O. H2	EDSE L.O. H2 (Arb. Unit)	Relative EDSE L.O. H2
Elastic	2±1	32±5	1.00	76±3	1.00
2^+	2.5±1	38±4	1.2±0.3	93±4	1.2±0.1
3^-	3.5±1	49±6	1.6±0.3	122±6	1.6±0.1

4.2 Calibration Technique

Using the above procedure to obtain the three peak positions in all combinations of strips and blocks allows for calibration of the light response, dL/dx, across these same components. We may change the normalization constant, C from the EDSE model (EQ.(30)), in order to reflect differences in the light response of the scintillator components. These differences are due to variations in gain in the electronics, quality of the optical connections, or attenuation of the light response along the length of individual strip scintillators.

$$\frac{dL}{dx} = C\frac{dN}{dx}\left(1 - \frac{F\frac{dN}{dx}}{A + \frac{dN}{dx}}\right) \quad \textbf{(30)}$$

The best-fit values of C for the horizontal strips and E blocks are shown in FIG. 27 and FIG. 28. Plotting the best-fit value of C relative to the distance from the optical connection gives information about the light response attenuation length. In the case of the strip scintillators, loss in the light response ranges between 10-20% over the entire active area of the strips. For the E blocks, the loss in the light response is approximately 5% over the entire active area.

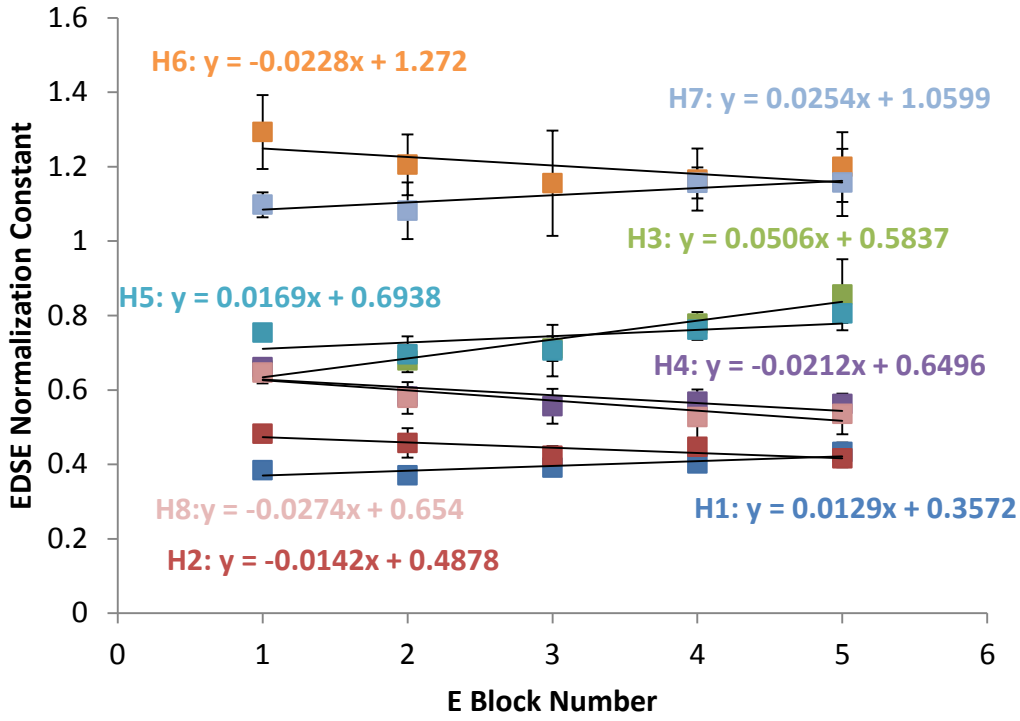

FIG. 27: Plot of the normalization constant C vs. horizontal strip number for the different E blocks.

The relationship between the energy deposited and the light response for individual scintillator components is shown in FIG. 29.

The light response curves for all combinations of strips and blocks may then be used to convert the raw measurement (as in FIG. 25) into histograms of the energy deposited (FIG. 30). Further analysis of these calibrated histograms provides information on the energy resolution of the strip and block scintillators.

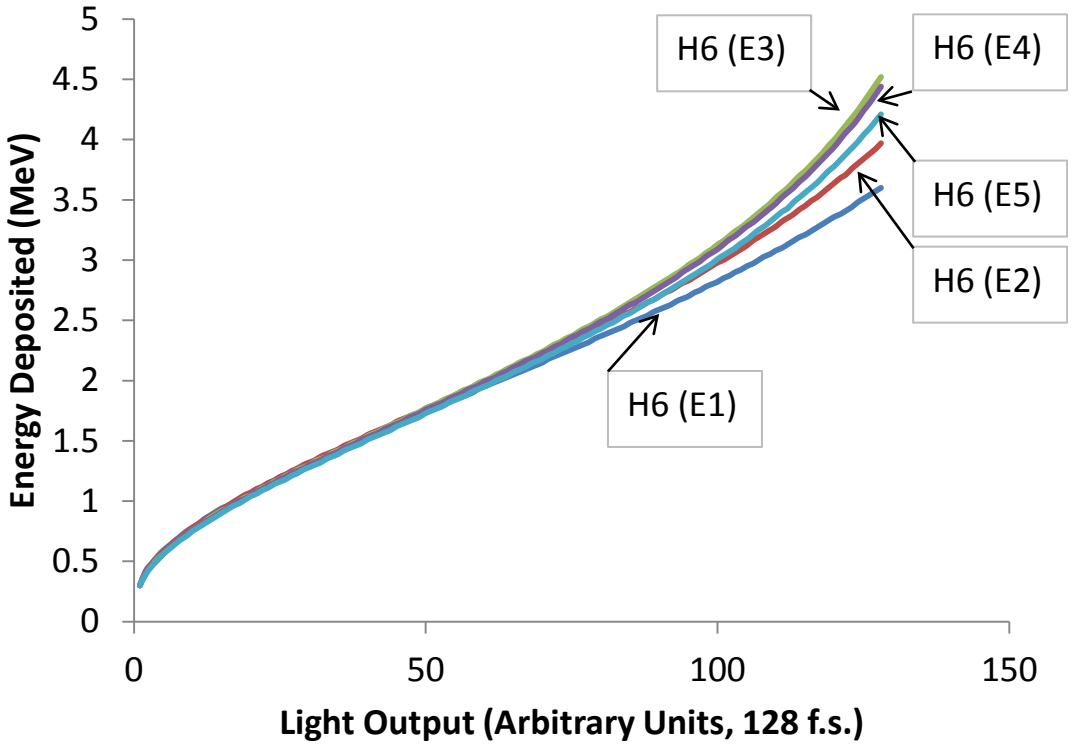

FIG. 28: Plot of calculated light output vs. energy for strip H6 in coincidence with E blocks 1 -5.

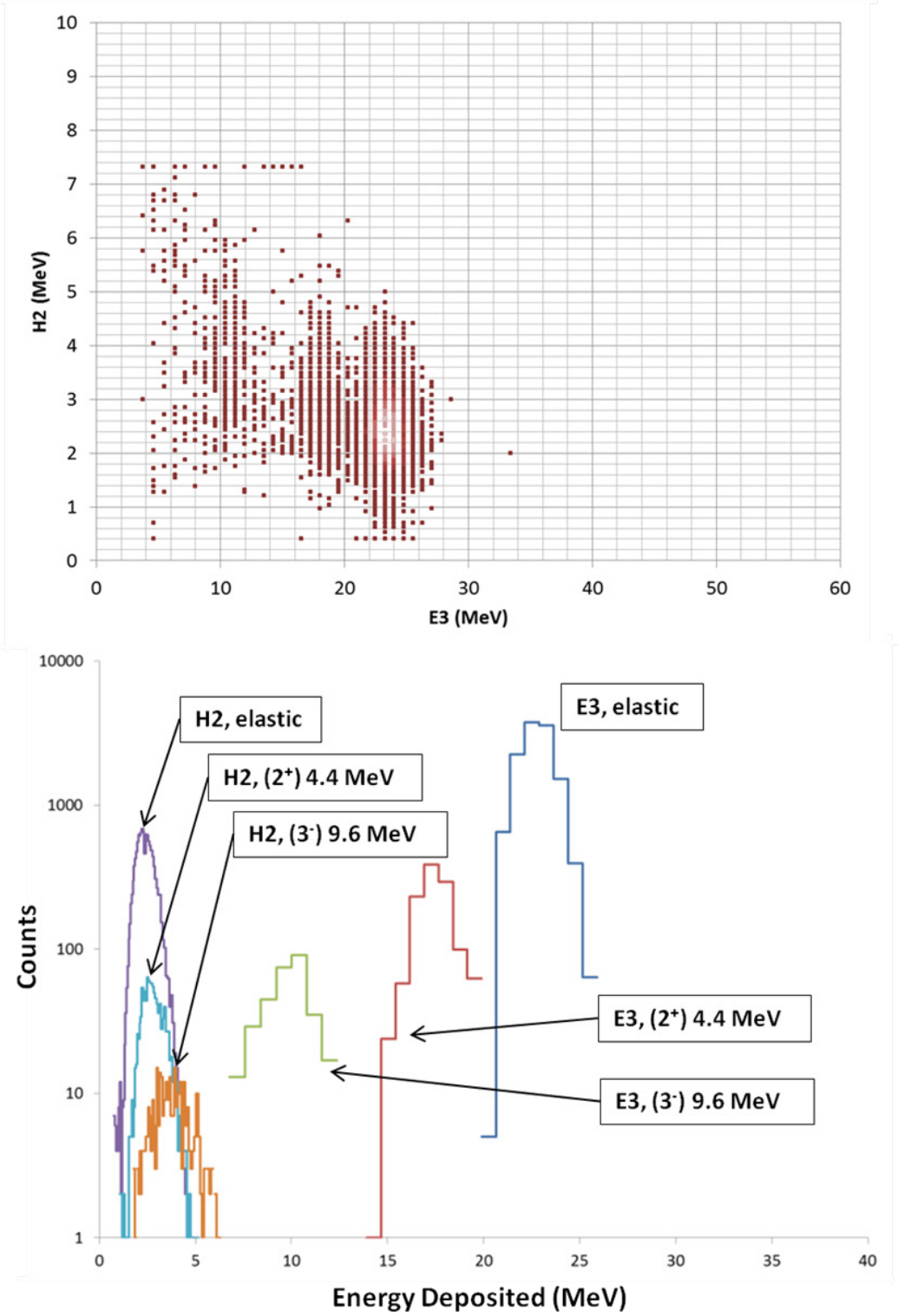

FIG. 29: Example of calibrated ΔE2-E 2D-spectrum and its 1D projections.

4.3 Energy Resolution

From the data, the energy resolution (Γ) (Full-Width at Half-Maximum (FWHM) of the peak [16]) of the strip and block scintillators is obtained. The energy resolution is affected by the spread in energy deposited as a result of small variations in the path length taken by the ion, which is referred to as energy straggling. Additionally, the energy resolution is affected by attenuation of the light response and by the different energies of incident protons. Energy straggling dominates in the strip scintillators.

The energy resolutions was obtained from Gaussian fits to the peaks in the energy spectra and is shown in FIG. 31.

For the strip scintillators, the resolution can be parameterized as $\Gamma/E = (21\pm5\%)\sqrt{E}$, where Γ is the FWHM and E is the average peak position. For the blocks, the resolution varied somewhat depending on the block but generally was 2.5 ±0.5MeV.

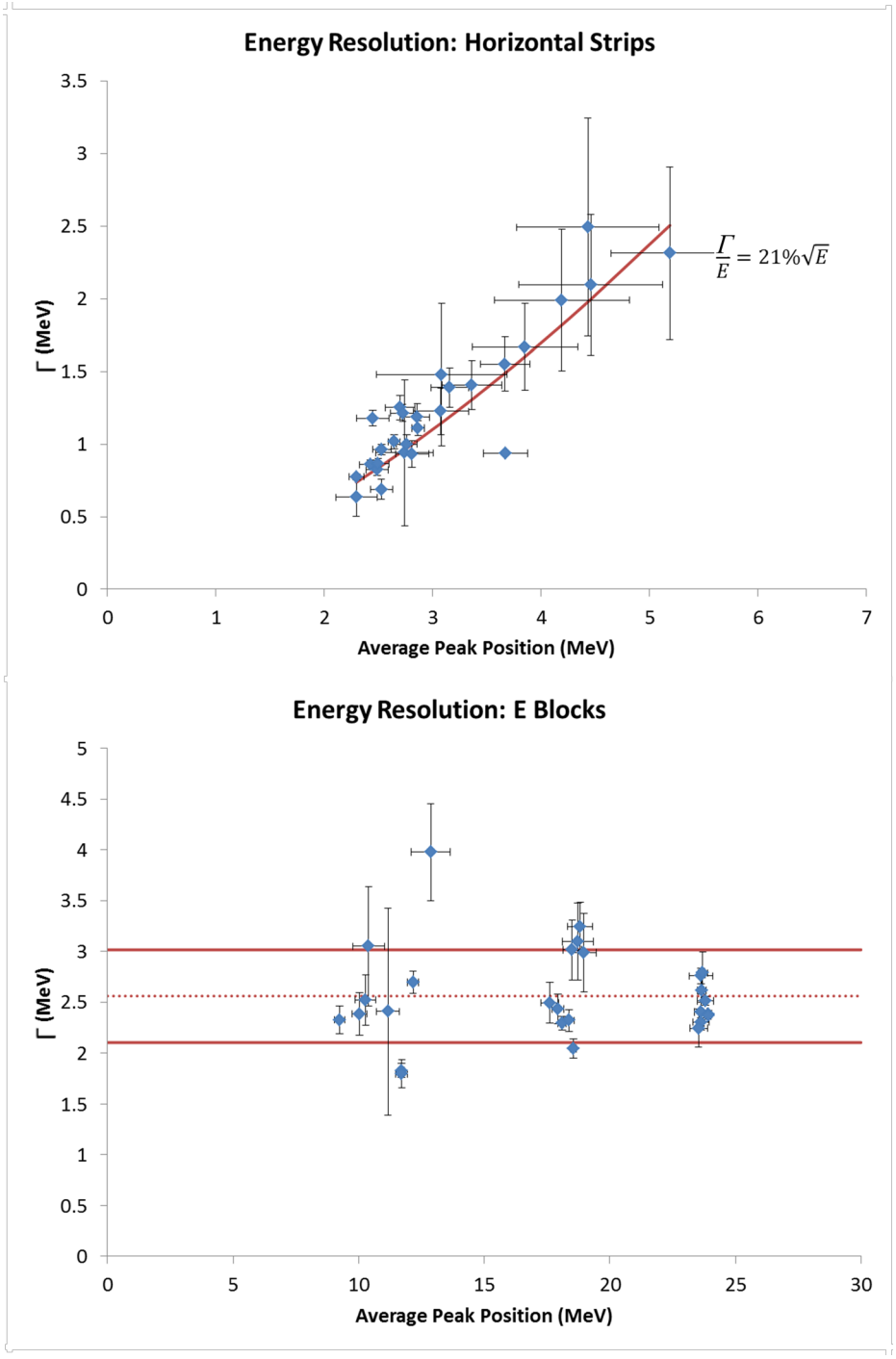

FIG. 30: Plots of the average peak position vs. Γ (FWHM) in strip and block scintillators.

The SRIM program, in addition to its stopping power and range tables, can be used to simulate the transport of ions through matter. This simulation is done using a Monte Carlo method. The target material is treated as amorphous, with its atoms uniformly distributed. The program calculates the trajectory of the incident ion after every nuclear and electronic collision with target atoms. This feature of SRIM was used to estimate the spread of energy deposited in a strip scintillator due to straggling. In order to make a comparison with the experimental measurement of the energy resolution, the simulation was run for a target material with 4 layers (aluminized Mylar wrap – strip scintillator – aluminized Mylar wrap – strip scintillator). Only considering ions with enough energy to reach the block layer, the energy deposited in the ΔE2 layer was calculated for each simulated ion. For a sample of 5000 simulated mono-energetic ions incident on the target material, the average and FWHM deposited energy was calculated and plotted in FIG. 32. Comparison of this result with the measurement shows that energy straggling accounts for approximately 60% of the energy resolution.

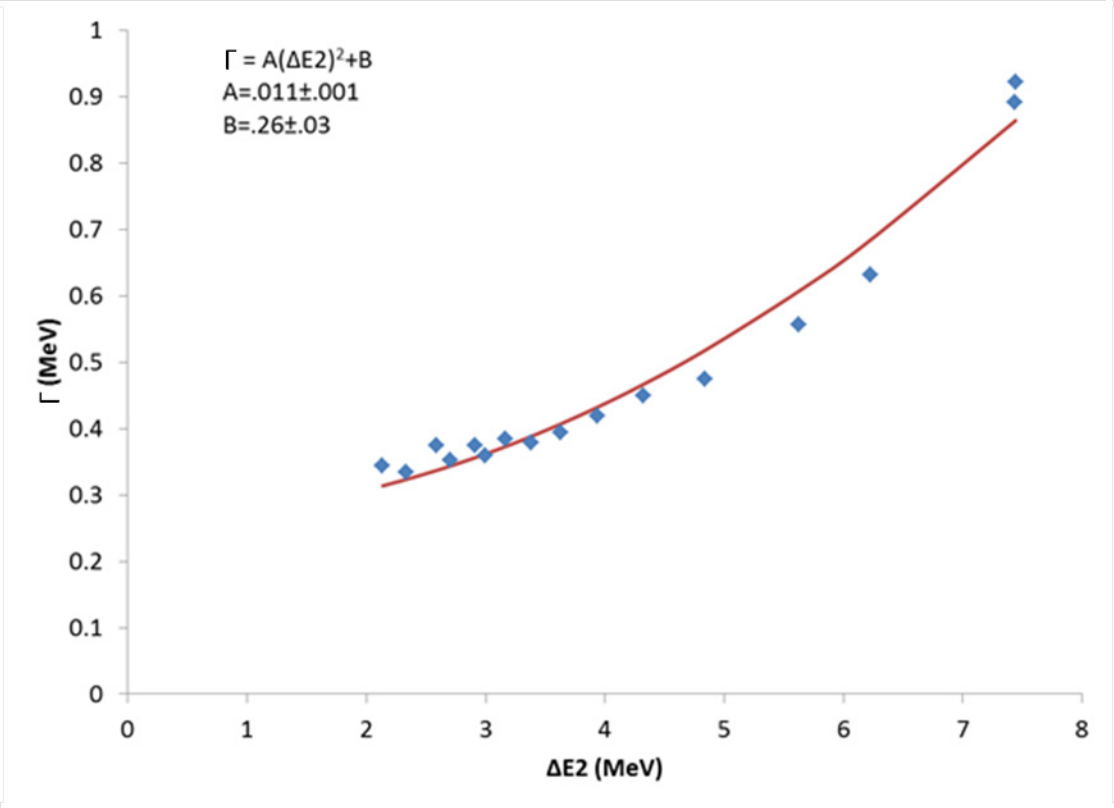

FIG. 31: ΔE2 vs. Γ, where ΔE2 is the average energy deposited by mono-energetic incident protons and Γ is the FWHM.

4.4 Attenuation Length

From the pixel geometry shown in FIG. 33, we know that the light response in the horizontal strips of the strip pairs which form the pixels should be the same (in the

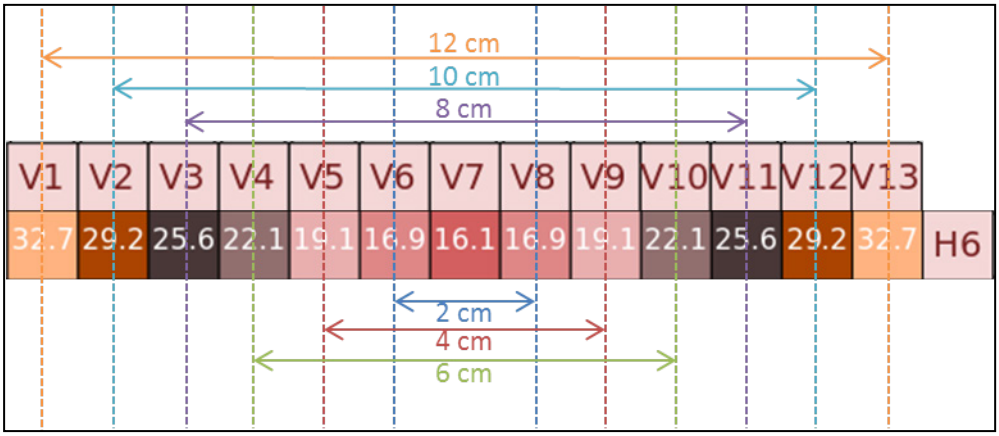

FIG. 32: Median distances between pixels that would have an equal light response in the absence of the attenuation.

absence of the attenuation effect) at equal distances, left or right, from the center. This is because those pixels lie at equal angles with respect to the beam direction and will have the same energy deposited. The attenuation length in the individual strips can then be measured by comparison of the light response from the symmetric pixel pairs about the detector center. This method has the advantage of not relying on estimates of the energy deposited. The energy resolution in the 2D ΔE1-ΔE2 spectra is too large to distinguish the different energy protons (FIG. 34). However, examining the 2D ΔE1-ΔE2 spectra is

advantageous for determining the attenuation length because of the smaller pitch between strip scintillators than between block scintillators.

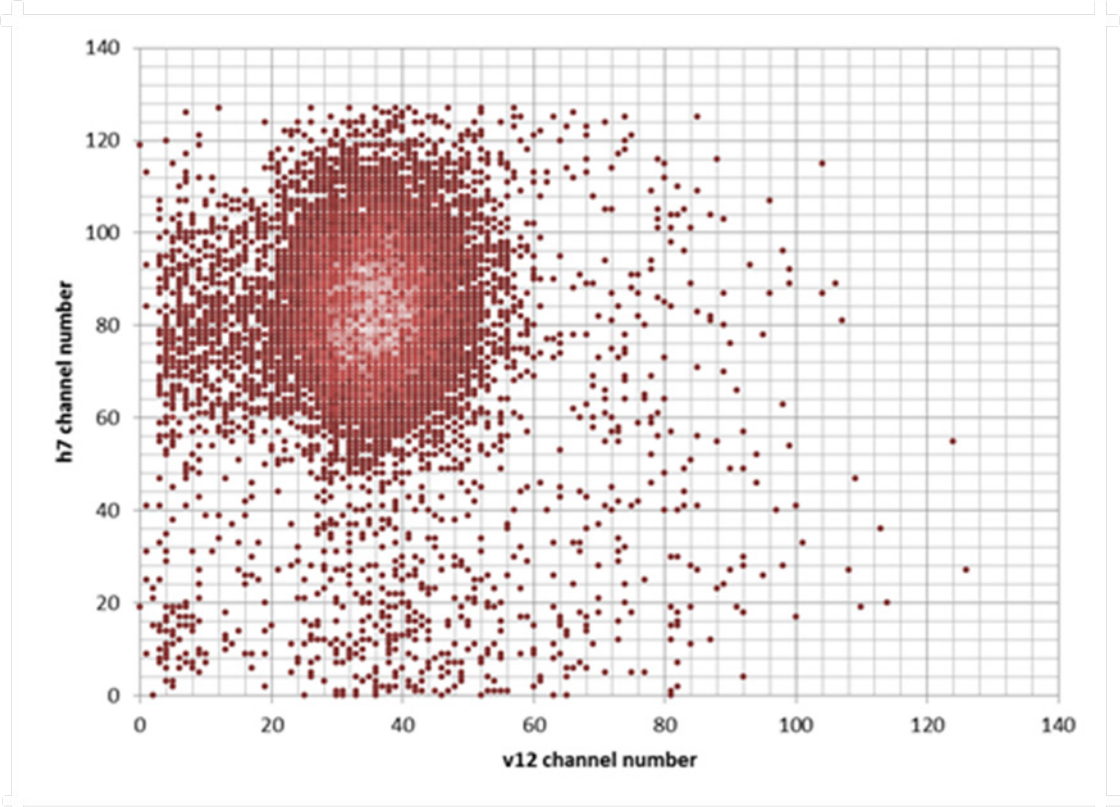

FIG. 33 An example ΔE1-ΔE2 2D-spectrum. The three peaks visible in the ΔE2-E 2D-spectra are not visible here due to the poorer energy resolution of the strip scintillators.

The ratio of the light response in the symmetric pixel pairs (relative light transmission = light response in the pixel further away from the optical connection / light response in the pixel closer to the optical connection) can be directly compared to the

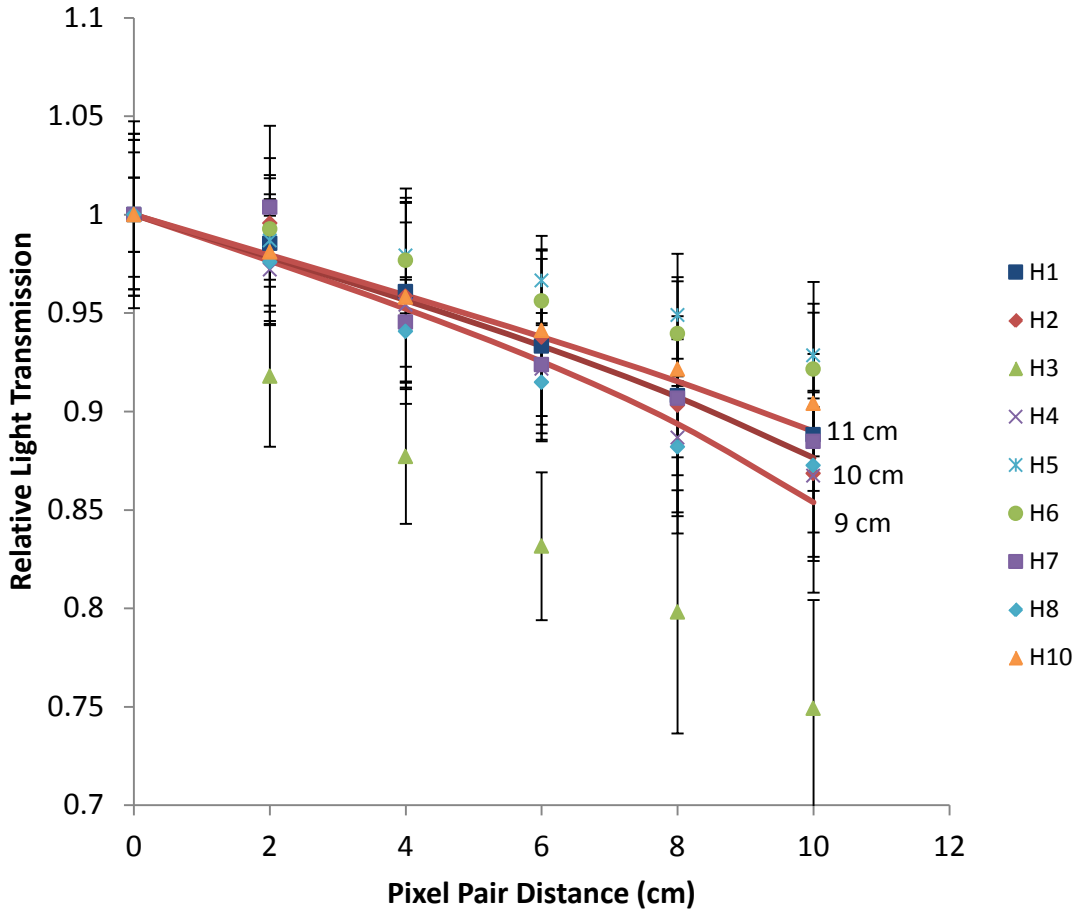

FIG. 34: Relative light transmission in horizontal strips vs. the distance between pixel pairs. The relative light transmission is the ratio of the light responses between the paired pixels. The pixel pair distance is described in FIG. 33. The plotted lines are the calculated values of the relative light transmission for varying distances (11 cm, 10 cm, and 9 cm) from the optical connection to the V7 strip.

result from the simulation of the attenuation behavior FIG. 24. The light response is taken to be the average peak position in the raw spectra and is shown in FIG. 35. The calculated ratios of the light responses are also shown in FIG. 35. The calculated ratios

assume λ_1 = 1.8 cm and λ_2 =104.3 cm. They are shown for varying values of the distance from the optical connection to the pixel coincident with vertical strip V7 (which sits at the center of the vertical strip array). This distance is difficult to measure precisely because when the strips are wrapped and installed onto the frame, the position of the optical connection is hidden from view. Consequently, the distance between the center of the array and the optical connection for the horizontal strips used to calculate this attenuation length has a large uncertainty and is taken to be 10±1 cm. The measurement fits within the calculated range in all but three of the horizontal strips (H3, H5, and H6). In strip H3, the transmission efficiency decays faster than expected. The best fit to the data from strip H3 gives attenuation lengths of λ_1 = 1.8 cm and λ_2 = 36.4 cm. Damage to the scintillator strip is a possible cause of the shorter attenuation length λ_2. In strips H5 and H6, the observed attenuation length, λ_2 = 165 cm, is much longer than expected but λ_1 = 1.8 cm in these strips as well. Further tests should be done with these strips in order to understand the cause of the better than expected performance.

4.5 Conclusion

Comparison of the light output of the E3 and H2 scintillators for protons from the three groups shows good agreement between the expected and experimental relative values. This method of comparison could be extended by applying a similar procedure to the 2D-spectra generated by coincidences between the ΔE1 and the E-Block layer. This would give an energy calibration for all scintillator signals.

The calibration was done by fitting the normalization constant in the EDSE model to the data. The normalization constant was extracted for horizontal strip and block pairs. Improvements to the calibration can be made by finding the normalization constant for each pixel formed by vertical and horizontal strips in coincidence with the pixel's corresponding block scintillator. Doing so would better account for the attenuation effect in the strip scintillators. Also, the relationship between the normalization constant and the pixel position along the length of the strip scintillator relative to the optical connection may be a sufficient method for measuring the attenuation length in the vertical strips.

Because of the poorer resolution in the strip scintillators, the three proton groups cannot be distinguished in the 2D histograms generated by coincidences between the ΔE1 and ΔE2 layers. However, for characterization purposes, the uncalibrated response by these layers in coincidence was used to make a finer measurement of the attenuation length of the light response. Analysis of the attenuation behavior as a function of the distance between symmetric pixel pairs showed that the majority of the horizontal strips are working as expected. The attenuation behavior should be measured consistently in this manner in order to ensure that the strips are in good condition.

The poorer resolution in the strip scintillators is due largely to the worse energy straggling in the thin strips, which accounts for approximately 60% of the observed energy resolution in the strips.

REFERENCES

[1] D. H. Youngblood, H. Clark, and Y. W. Lui, Phys. Rev. C **57**, 1134 (1998).

[2] M. N. Harakeh, A. Van Der Woude, *Giant Resonances: Fundamental High-Frequency Modes of Nuclear Excitation* (Oxford University Press, New York, NY, 2001).

[3] P. A. Assimakopoulos and N. H. Gangas, Nucl. Instrum. Methods **47**, 260 (1967).

[4] W. Cheney and D. Kincaid, *Numerical Mathematics and Computing* (Thomson Brooks/Cole, Belmont, CA, 2008), p. 96-99.

[5] G. G. Ohlsen, Nucl. Instrum. Methods **37**, 240 (1965).

[6] X. Chen, Y. Lui, H. Clark, Y. Tokimoto, and D. Youngblood, *Giant Resonance Study by ^{6}Li Scattering* (Texas A&M University, College Station, TX, 2010).

[7] J. F. Ziegler, M. Ziegler, and J. Biersack, Nucl. Instrum. Methods **268**, 1818 (2010).

[8] J. Birks, Phys. Rev. **86** (1952).

[9] K. Michaelian, A. Menchaca-Rocha, and E. Belmont-Moreno, Nucl. Instrum. Methods **356**, 297 (1995).

[10] Saint-Gobain Ceramics & Plastics, Inc., *Saint-Gobain Ceramics & Plastics, Inc. BC 400-404-408-412-416 Data Sheet*, 2008), 2012.

[11] J. Lindhard, M. Scharff, and H. E. Schiott, Mat. Fys. Medd. Dan **33**, 14 (1963).

[12] T. Everhart, J. Appl. Phys. **31**, 1483 (1960).

[13] K. Kanaya and S. Okayama, Appl.Phys,(J. Phys. D) **5**, 43 (1972).

[14] F. Becchetti, C. Thorn, and M. Levine, Nucl. Instrum. Methods **138**, 93 (1976).

[15] National Nuclear Data Center, *National Nuclear Data Center, information extracted from the Chart of Nuclides database,* http://www.nndc.bnl.gov/chart/ (2012).

[16] J. Beringer et al. (Particle Data Group), Phys. Rev. D**86**, 010001 (2012).